Journal of *Marine Science and Engineering*

MDPI

Article

Effect of Guide Vane Case on Hydrodynamic Performance and Unsteady Pressure-Pulsation Characteristics of Shaftless Pump-Jet Thruster

Taofeng Wang [1,2], Sanming Song [2,*], Liming Li [2,3], Jinxing Yu [1,2], Kaizhou Liu [4,5], Adam Rushworth [3] and Xisheng Feng [4,5]

1 College of Mechanical and Control Engineering, Guilin University of Technology, Guilin 541006, China; tf.wang@siat.ac.cn (T.W.)
2 Shenzhen Institutes of Advanced Technology, Chinese Academy of Sciences, Shenzhen 518055, China; liming.li@nottingham.edu.cn
3 Faculty of Science and Engineering, University of Nottingham Ningbo China, Ningbo 315100, China; adam.rushworth@nottingham.edu.cn
4 Institutes for Robotics and Intelligent Manufacturing, Chinese Academy of Sciences, Shenyang 110169, China; fxs@sia.cn (X.F.)
5 State Key Laboratory of Robotics and Intelligent Systems, Shenyang Institute of Automation, Chinese Academy of Sciences, Shenyang 110016, China
* Correspondence: sm.song@siat.ac.cn

Abstract

Propulsors are essential power units for underwater vehicles and major sources of self-noise, with unsteady pressure pulsations linked to flow-induced noise. To study the impact of guide vane case on the hydrodynamic performance and pressure pulsation of a shaftless pump-jet thruster, six guide vane configurations were first compared under a reference operating condition of 600 rpm: a vaneless baseline, fixed vertical guide vanes, fixed forward-inclined guide vanes, fixed reverse-inclined guide vanes, co-rotating guide vanes, and counter-rotating guide vanes. Based on this comparison, the vertical-vane and counter-rotating-vane configurations were selected for extended operating-condition analysis under three rotational speeds and three inflow conditions. Transient numerical simulations were conducted using the SST $k-\omega$ turbulence model. The rotating regions were defined in a rotating reference frame, and the unsteady rotor–stator interaction was resolved using a transient sliding-mesh interface. Results show that the counter-rotating guide vane configuration achieves the highest head and efficiency among the tested cases, with a head of 1.8955 m and efficiency of 0.7306, representing increases of 19.64% and 22.87% over the fixed vertical guide vane case. The fixed forward-inclined guide vane exhibits the strongest thrust fluctuation and pressure pulsation. Pressure-pulsation intensity generally decreases from the impeller rim toward the central axis. Frequency-domain results indicate that most cases are dominated by the blade-passing frequency, whereas the counter-rotating guide vanes show a response nearly twice this frequency.

Keywords: shaftless pump-jet thruster; numerical simulation; guide vane orientation; pressure pulsation; frequency-domain analysis

Check for updates

Academic Editors: Decheng Wan, Mai The Vu, Caoyang Yu, Anh Tuan Vo and Gong Xiang

Received: 7 July 2026
Revised: 8 August 2026
Accepted: 12 August 2026
Published: 14 August 2026

Copyright: © 2026 by the authors. Licensee MDPI, Basel, Switzerland. This article is an open access article distributed under the terms and conditions of the Creative Commons Attribution (CC BY) license.

1. Introduction

With the rapid development of the modern shipbuilding industry, shaftless pump-jet thrusters (SPTs) have been widely applied in both military and civilian fields owing to their

distinctive advantages. Compared with conventional propellers or shaft-driven pump-jet propulsors, SPTs eliminate the transmission shaft running through the vehicle and employ a rim motor to directly drive the rotor, thereby substantially simplifying the structural layout and improving system integration [1].

Previous open-water investigations have also shown that shaftless pump-jet thrusters have their own hydrodynamic characteristics and operating range, which should be considered separately from conventional propulsors [2]. Because of their compact structure, low operating noise, and high efficiency, SPTs have become a promising propulsion solution for underwater vehicles such as submarines, autonomous underwater vehicles, and underwater robots.

A shaftless pump-jet thruster generally consists of an inlet, a rotor or impeller, guide vanes or stators, and a nozzle. Among these components, the guide vanes not only rectify the incoming flow so that it enters the rotor blades at a more favorable angle of attack, thereby enhancing the energy conversion capability or efficiency of the rotor, but also play an important role in suppressing inlet backflow and flow separation, as well as reducing flow-induced noise and structural vibration. Therefore, the geometry, installation angle, and matching relationship between the guide vanes and the rotor directly determine the hydrodynamic and acoustic performance of the propulsion system. For example, duct-geometry studies on pump-jet propulsors have shown that local geometric parameters can significantly affect hydrodynamic performance, confirming that component case should be treated as a quantitative design variable rather than only as a qualitative flow-control factor [3]. The noise sources of SPTs mainly include mechanical vibration noise, electromagnetic interference noise, and hydrodynamic noise, among which flow-induced noise caused by pressure fluctuations resulting from unsteady blade loading is generally dominant. Accordingly, an in-depth understanding of the internal flow mechanism and pressure-pulsation characteristics of SPTs is important for preliminarily evaluating flow-induced noise risk and supporting subsequent low-noise design studies [4].

Early studies on pump-jet guide vanes were mainly focused on shaft-driven cases. Weng et al. carried out towing-tank and cavitation-tunnel experiments as well as CFD calculations for a self-designed pre-stator pump-jet propulsor with nine rotor blades, 13 stator blades, a rotor diameter of 204.85 mm, and a tip clearance of 1 mm. Their results showed good agreement between numerical and experimental hydrodynamic/noise predictions, and the calculated sound-pressure spectra exhibited clear line components at the shaft frequency, blade frequency, and their harmonics, with a pronounced high-frequency peak at 26 fb = 3744 Hz [5]. These results provide a more specific quantitative basis than the general statement that guide vanes can improve pump-jet performance.

With the development of shaftless pump-jet propulsion, guide vane design faces new challenges and opportunities. Because the central transmission shaft is removed, the internal flow passage of an SPT becomes more compact, and the guide vanes are often directly integrated into the hub or duct wall. This restricts the freedom of spatial arrangement and requires simultaneous consideration of electromagnetic component layout, bearing lubrication paths, and clearance-flow control. He et al. showed that clearance-flow design and bearing arrangement are important in shaftless pump-jet thrusters, indicating that guide vane structures must be coordinated with the bearing and clearance layout to avoid interference and maintain smooth internal flow [6]. Shen et al. further demonstrated that the integrated motor layout of a shaftless pump-jet propulsor imposes additional constraints on the available hub-region installation space [7]. In this context, even slight adjustments in guide vane orientation may induce pronounced changes in clearance flow, secondary flow, or local backflow, thereby affecting the overall performance.

In recent years, increasing attention has been paid to the internal flow characteristics of SPTs and the role of local flow loss. Cao et al. compared shaft-driven and shaftless water-jet propulsion systems and reported that the shaftless case achieved nearly a 2% performance improvement under the design condition, mainly because removal of the upstream shaft reduced inlet velocity circulation and weakened local separation [8]. Lei et al. investigated cavitation flow and flow loss in a shaftless water-jet propulsion pump under different acceleration conditions; their validation reported an experimental uncertainty below plus or minus 0.866% and simulation deviations of less than 5%. They further showed that the cavity-volume increment was 0.01544 under linear acceleration but only 0.00414 under exponential acceleration, with a maximum difference of 0.01124 between the two profiles, and that the dominant frequencies at the monitoring locations were associated with the shaft frequency and its seventh harmonic [9]. Han et al. also showed that a local geometric parameter can produce measurable effects on hydraulic performance: an optimal gap coefficient of 0.15 produced a peak efficiency of 75% and a head of 1.9 m under low-flow conditions [10].

In terms of numerical simulation, Zhu et al. established experimental and numerical methods for a rim-driven thruster and showed that the head curve had a hump characteristic, with the maximum head obtained at $Q = 600\ m^3/h$. Their internal flow analysis further indicated that, as the flow rate decreased, large-scale backflow gradually appeared near the wall upstream of the impeller inlet, in the central region downstream of the impeller, and on both sides of the central low-pressure zone, causing increased flow loss and a drop in head [11]. Li et al. studied the hydrodynamic performance of an integrated motor pump-jet thruster with gap-flow effects and found that, among the axial-gap cases, the minimum efficiency occurred at an axial gap of 2 mm whereas the maximum efficiency occurred at 4 mm; among the radial-gap cases, the minimum efficiency occurred at a radial gap of 2 mm [12]. These studies indicate that local case parameters, even when not directly treated as guide vane variables, can significantly influence performance and internal flow organization.

Meanwhile, vibration and noise control has become another core objective in pump-jet design. Huang et al. showed that surface roughness can alter pump-jet hydrodynamics and flow-noise behavior, indicating that near-wall flow conditions are important for noise-sensitive pump-jet design [13]. These studies further suggest that the design of guide vanes should be linked not only to mean performance, but also to pressure pulsation and vibration/noise response.

Related studies on axial-flow and rotor–stator hydraulic machinery also provide useful support for the present guide vane problem. Yevtushenko et al. investigated an axial-flow pump stage composed of guide vanes, an impeller, and a diffuser; using both experiments and CFD for three impellers over six capacities, they showed that both pump performance curves and downstream velocity distributions depended strongly on guide vane/impeller matching [14]. Binama et al. investigated ten operating conditions in a reversible pump–turbine and showed that pressure-pulsation amplitude in the vaneless space increased as runner blade number decreased from nine to seven, while instability transmission was more pronounced toward upstream flow regions [15]. Nouri et al. experimentally studied a ducted counter-rotating axial-flow stage and found that the relative rotation-rate ratio and axial spacing strongly affected overall performance, while increasing the spacing from 17% to 310% caused only a small decrease in efficiency [16]. Although these studies are not focused on shaftless pump-jet thrusters, they support the physical relevance of guide vane/rotor matching, relative motion, and rotor–stator interaction in the present work.

Additional pump-jet and ducted propulsor studies also show that propulsion performance can be sensitive to case and operating condition. Odetti et al. designed and constructed a modular pump-jet thruster for shallow-water operations and emphasized the importance of loss estimation and propulsion-system integration in practical pump-jet design [17]. Zhang et al. investigated a ducted propeller under oblique flow from 15 degrees to 60 degrees and showed that blade and nozzle loads vary markedly with inflow incidence, further indicating that ducted propulsion performance is sensitive to geometry and operating condition [18].

Classical pump-design variables are also useful for explaining why such changes should be expected. In conventional pump theory, specific speed provides a first-order operating descriptor of the relationship among rotational speed, flow rate, and head [19]. For the present SPT, the reference specific-speed estimate is used only to characterize the prescribed simulated operating condition, but it still helps clarify why guide vane/impeller matching should be discussed using axial-flow pump theory. Even though the present study does not perform a full design optimization based on these variables, they remain physically important because a change in guide vane handedness or motion state alters the local prewhirl and the effective flow-turning process seen by the impeller. In turn, the actual rotor loading may deviate from the idealized design condition, producing different levels of residual swirl, loss, and unsteady excitation. In this sense, the present problem is closely connected to the classical issues of velocity-triangle matching, deviation or slip from ideal flow turning, and rotor–stator interaction in axial-flow machinery [8].

In summary, existing studies have revealed the important role of guide vanes and local geometric parameters in pump-jet propulsion systems from the perspectives of flow rectification, clearance flow, cavitation, vibration, and noise. However, for the highly integrated shaftless pump-jet case, most available studies have focused on overall shaftless-versus-shaft-driven performance, baseline open-water or internal flow characteristics, clearance or structural-layout effects, or cavitation/noise issues in a broader sense. Quantitative comparisons of the relationships among impeller performance, internal pressure distribution, and pressure-pulsation spectra under different guide vane cases and motion states remain insufficient. In contrast to studies that mainly address overall performance differences or local gap/cavitation effects, the present study focuses on how guide vane type, rotational direction, and motion state affect the unsteady pressure characteristics and energy performance of an SPT. This work is motivated by the demand for low-self-noise underwater vehicles, for which propulsion systems must provide adequate thrust while minimizing pressure-pulsation-related noise sources. Therefore, before prototype development, preliminary hydrodynamic and pressure-pulsation analyses are needed to evaluate feasible pump-jet configurations.

Therefore, this study conducts a comparative investigation of six guide vane cases, with particular attention on the following questions: how different guide vane cases affect impeller head, efficiency, and thrust coefficient; how guide vane case modifies the low-pressure distribution on the impeller suction surface and within the internal flow field of the pump-jet; how pressure-pulsation intensity and dominant frequency vary at different radial monitoring points; and why the counter-rotating guide vane case induces a response at twice the blade-passing frequency. The six guide vane configurations were first evaluated under a unified reference condition to identify representative hydrodynamic and pressure-pulsation characteristics. To further assess operating-condition sensitivity, the vertical-vane and counter-rotating-vane configurations were subsequently analyzed under three rotational speeds and three inflow conditions.

2. Research Model and Numerical Methodology

2.1. Three-Dimensional Modeling

Tan et al. [20] numerically investigated the influence of blade number on the performance of a shaftless pump-jet thruster model and found that the head, efficiency, and thrust of the thruster increased gradually as the blade number increased from five to seven. Therefore, in the present study, a shaftless pump-jet thruster equipped with a seven-bladed impeller is selected as the research object. The main parameters of the simulated thruster are as follows: reference rotational speed $n = 600$ rpm, impeller diameter $D = 324$ mm, number of impeller blades $n_1 = 7$, hub-to-tip radius ratio $r_h = 0.25$, and number of guide vane blades $n_2 = 7$, with a blade setting angle of 0°. The impeller is arranged in the downstream section of the duct, whereas the guide vane device is installed in the upstream section. The three-dimensional geometric model of the simplified shaftless pump-jet thruster surrogate is shown in Figure 1, in which the main components include the duct, guide vane, and impeller.

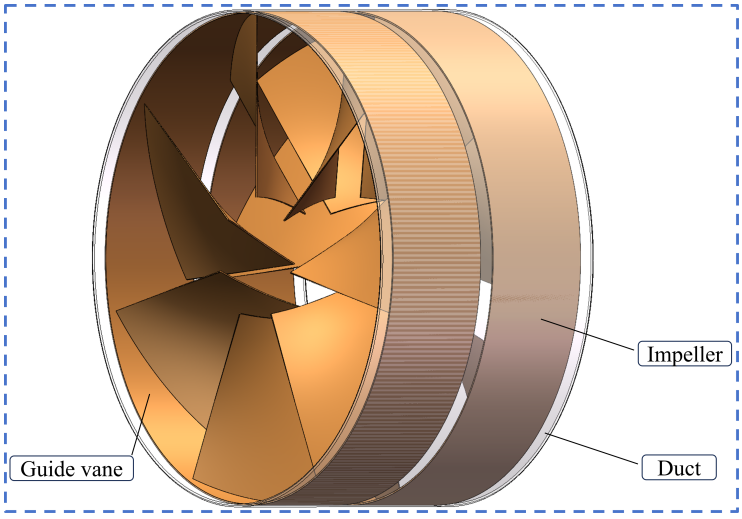


Figure 1. The three-dimensional geometric model of the simplified shaftless pump-jet thruster surrogate.

In this study, the guide vane with the same geometric handedness as the working impeller blade is denoted as Blade Type 1, whereas that with the opposite geometric handedness is denoted as Blade Type 2. The surrogate models of the impeller and guide vane device are shown in Figure 2.

To ensure geometric reproducibility, the principal dimensions of the shaftless pump-jet thruster are summarized in Table 1. In the present study, the impeller blade and guide vane are represented by surrogate blades of uniform thickness rather than by conventional airfoil sections. The blade thickness is $t = 1$ mm, the characteristic chord length is $c = 60$ mm, and the imposed twist angle used to generate the blade surface is $\theta = 60°$. The axial spacing between the guide vane trailing edge and the impeller leading edge is $s_{rs} = 80$ mm. Because the present shaftless rotor adopts a rim-connected blade case, no conventional free blade-tip gap is defined in the model. Blade Type 1 denotes the guide vane with the same geometric handedness as the impeller blade, whereas Blade Type 2 denotes the guide vane with the opposite handedness.

It should be emphasized that the present guide vane cases are simplified surrogate models intended for controlled comparative analysis rather than for practical rotor–stator optimization based on classical velocity-triangle matching. In the present study, the guide vane with the same handedness as the impeller and the guide vane with the opposite handedness were introduced to isolate the effect of handedness while keeping the principal geometric parameters, such as blade thickness, chord length, diameter, and twist angle,

unchanged. Likewise, the guide vane blade number was set equal to the impeller blade number ($n_2 = n_1 = 7$) to avoid introducing an additional blade-number variable into the six-case comparison. This choice provides a consistent geometric and numerical basis for comparing handedness and motion state.

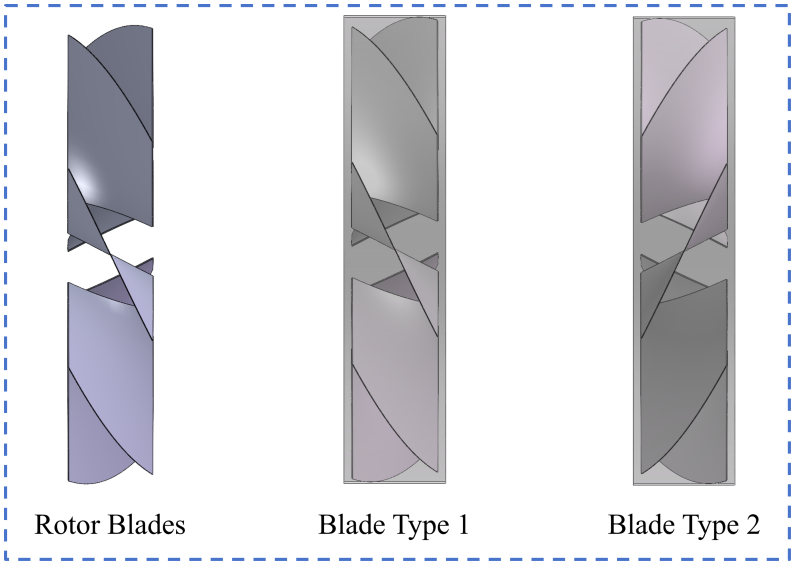


Figure 2. Three-dimensional models of the impeller and guide vane assembly. The guide vanes sharing the same handedness as the impeller are designated as Blade Type 1, while those with the opposite handedness are designated as Blade Type 2.

Table 1. Geometric definition of the simplified surrogate blade.

Item	Symbol	Value
Uniform blade thickness	t	1 mm
Characteristic blade chord	c	60 mm
Impeller diameter	D	324 mm
Hub-to-tip radius ratio	r_h	0.25
Twist angle	θ	60°
Conventional free tip gap	g_{tip}	not applicable
Rotor–stator axial gap	s_{rs}	80 mm

2.2. Simulation Cases

In this study, six simulation cases were designed according to the geometric handedness and motion state of the guide vanes relative to the rotating blades of the working impeller, as listed in Table 2. For the rotating guide vane cases, a rotational speed of 600 rpm was assigned to the guide vanes.

Table 2. Guide vane cases.

Case	Guide Vane Type	Guide Vane State	Relationship with Impeller Blade Handedness
Case 1	Vaneless baseline	None	None
Case 2	Vertical guide vane	Fixed	No handedness
Case 3	Blade 1 guide vane	Fixed	Same handedness
Case 4	Blade 2 guide vane	Fixed	Opposite handedness
Case 5	Blade 1 guide vane	Rotating	Same handedness, 600 rpm
Case 6	Blade 2 guide vane	Rotating	Opposite handedness, 600 rpm

2.3. Numerical Model and Boundary Conditions

The transient flow-field simulations were performed using OpenFOAM with the SST $k-\omega$ turbulence model. This model can adequately account for shear-stress transport

near solid walls and effectively capture near-wall flow characteristics, thereby providing improved predictive accuracy for complex flow fields [21]. A second-order upwind scheme was used for the spatial discretization of the convection terms. For temporal discretization, a second-order implicit unsteady scheme was adopted. The convective Courant number was monitored during the transient simulations. The volume-averaged convective Courant number was approximately 1.29×10^{-2}, supporting the suitability of the selected time-step size for resolving the transient flow evolution under the present implicit unsteady calculation. The total number of time steps was set to 7200, with 36,000 numerical iterations performed during the calculation, and the resulting data were post-processed, plotted, and frequency-analyzed using Origin 2024. The time-averaged continuity equation and Reynolds-averaged Navier–Stokes (RANS) equations for separated incompressible flow were employed as the governing equations [22]. The continuity and momentum equations are expressed as follows:

$$\frac{\partial \bar{u}_i}{\partial x_i} = 0 \tag{1}$$

$$\rho \frac{\partial \bar{u}_i}{\partial t} + \rho \bar{u}_j \frac{\partial \bar{u}_i}{\partial x_j} = -\frac{\partial \bar{p}}{\partial x_i} + \frac{\partial}{\partial x_j}\left[(\mu + \mu_t)\left(\frac{\partial \bar{u}_i}{\partial x_j} + \frac{\partial \bar{u}_j}{\partial x_i}\right)\right] + \bar{S}_i \tag{2}$$

$$\rho \frac{\partial \bar{u}_i}{\partial t} + \rho \bar{u}_j \frac{\partial \bar{u}_i}{\partial x_j} = -\frac{\partial \bar{p}}{\partial x_i} + \frac{\partial}{\partial x_j}\left[(\mu + \mu_t)\left(\frac{\partial \bar{u}_i}{\partial x_j} + \frac{\partial \bar{u}_j}{\partial x_i}\right)\right] \tag{3}$$

The turbulence closure is provided by the SST $k-\omega$ two-equation model. The corresponding transport equations for turbulent kinetic energy k and specific dissipation rate ω are as follows:

$$\frac{\partial(\rho k)}{\partial t} + \frac{\partial(\rho \bar{u}_j k)}{\partial x_j} = \frac{\partial}{\partial x_j}\left[\left(\mu + \frac{\mu_t}{\sigma_k}\right)\frac{\partial k}{\partial x_j}\right] + P_k - \beta^* \rho \omega k + S_k \tag{4}$$

$$\frac{\partial(\rho k)}{\partial t} + \frac{\partial(\rho \bar{u}_j k)}{\partial x_j} = \frac{\partial}{\partial x_j}\left[\left(\mu + \frac{\mu_t}{\sigma_k}\right)\frac{\partial k}{\partial x_j}\right] + P_k - \beta^* \rho \omega k \tag{5}$$

$$\frac{\partial(\rho \omega)}{\partial t} + \frac{\partial(\rho \bar{u}_j \omega)}{\partial x_j} = \frac{\partial}{\partial x_j}\left[\left(\mu + \frac{\mu_t}{\sigma_\omega}\right)\frac{\partial \omega}{\partial x_j}\right] + \alpha \frac{\omega}{k} P_k - \beta \rho \omega^2 + S_\omega + 2(1 - F_1)\frac{\rho}{\sigma_{\omega 2}}\frac{1}{\omega}\frac{\partial k}{\partial x_j}\frac{\partial \omega}{\partial x_j} \tag{6}$$

$$\begin{aligned}\frac{\partial(\rho \omega)}{\partial t} + \frac{\partial(\rho \bar{u}_j \omega)}{\partial x_j} =& \frac{\partial}{\partial x_j}\left[\left(\mu + \frac{\mu_t}{\sigma_\omega}\right)\frac{\partial \omega}{\partial x_j}\right] + \alpha \frac{\omega}{k} P_k - \beta \rho \omega^2 \\ &+ 2(1 - F_1)\frac{\rho}{\sigma_{\omega 2}}\frac{1}{\omega}\frac{\partial k}{\partial x_j}\frac{\partial \omega}{\partial x_j}\end{aligned} \tag{7}$$

For clarity, the variables and model coefficients appearing in Equations (1)–(4) are summarized in Table 3.

The turbulent viscosity μ_t is defined as

$$\mu_t = \frac{\rho a_1 k}{\max(a_1 \omega, \Omega F_2)} \tag{8}$$

where $\Omega = \sqrt{2\Omega_{ij}\Omega_{ij}}$ is the magnitude of the vorticity, $\Omega_{ij} = \frac{1}{2}\left(\frac{\partial \bar{u}_i}{\partial x_j} - \frac{\partial \bar{u}_j}{\partial x_i}\right)$, and F_2 is a blending function introduced to address the issue of excessively low turbulent viscosity μ_t in free shear flows.

Table 3. Definitions of variables and model coefficients in Equations (1)–(4).

Symbol	Unit	Definition
x_i, x_j	m	Cartesian coordinate directions; repeated indices follow Einstein summation convention.
t	s	Time.
$\bar{u}_i, \bar{u}_j$	m/s	Time-averaged velocity components in the i- and j-directions.
ρ	kg/m^3	Fluid density.
$\bar{p}$	Pa	Time-averaged pressure.
μ	Pa·s	Dynamic viscosity of the fluid.
μ_t	Pa·s	Turbulent viscosity.
k	m^2/s^2	Turbulent kinetic energy.
ω	s^{-1}	Specific dissipation rate.
P_k	kg/(m·s^3)	Production term of turbulent kinetic energy.
$\sigma_k, \sigma_\omega, \sigma_{\omega 2}$	–	Turbulent Prandtl-type constants in the SST $k-\omega$ model.
α, β, β^*	–	Closure coefficients in the SST $k-\omega$ model.
F_1	–	Blending function used in the SST $k-\omega$ model.

In the present study, the rotating impeller region and the rotating guide vane region in the corresponding cases were defined in a rotating reference frame. Since the moving components undergo prescribed rigid-body rotation without blade deformation, a fully dynamic mesh was not adopted. For the present rotor–stator problem, a fully dynamic mesh would require continuous mesh deformation or remeshing to accommodate the relative rotation between stationary and rotating domains, which may introduce additional cell-quality variation, interpolation uncertainty, and substantially higher computational cost during long-time transient calculations. Therefore, a transient rotor–stator interface was adopted to resolve the unsteady interaction while maintaining stable mesh quality. The transient rotor–stator interfaces were arranged at the upstream and downstream boundaries of the downstream impeller rotating region. For the dynamically rotating guide vane cases, additional transient rotor–stator interfaces were arranged at the upstream and downstream boundaries of the upstream rotating guide vane region. The same interface-placement criterion and grid topology were applied consistently among the corresponding cases, so that the comparative differences among guide vane configurations were evaluated under the same numerical treatment. The inlet was specified as a velocity inlet, and the outlet was defined as a pressure outlet [23]. The dimensions of the three-dimensional computational domain are shown in Figure 3.

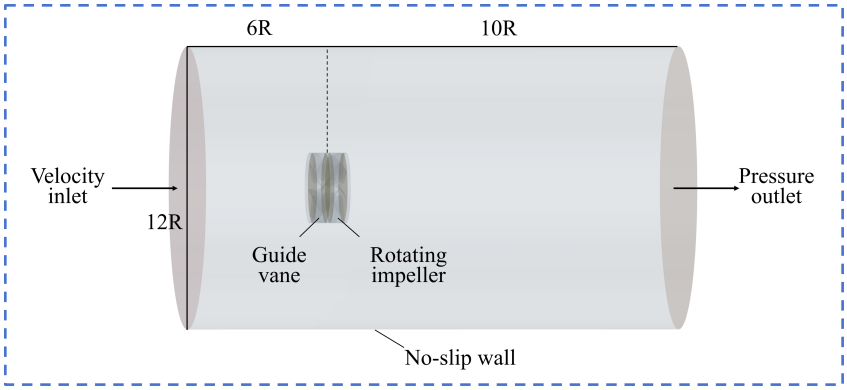


Figure 3. Three-dimensional computational domain.

After defining the computational domain and boundary conditions, a set of monitoring points was arranged between the guide vanes and the working impeller to investigate the variation in internal pressure pulsations in the shaftless pump-jet thruster under different

guide vane cases. This set consisted of three monitoring points uniformly distributed along the radial direction of the pump-jet from the impeller rim toward the central axis, denoted as M1, M2, and M3, respectively. Taking the pump-jet model with fixed vertical guide vanes in Case 2 as an example, the specific locations of the monitoring points are shown in Figure 4.

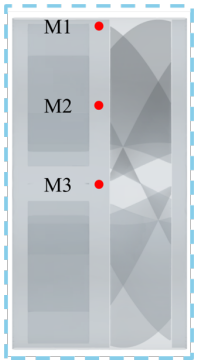


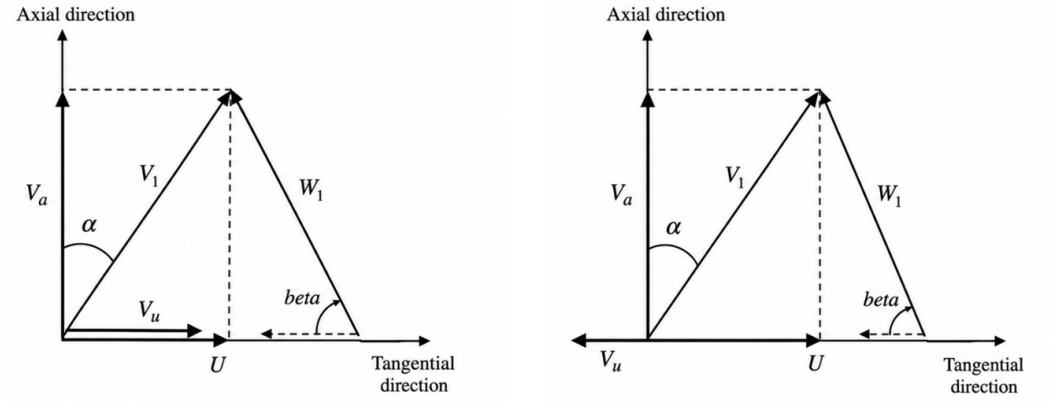
Figure 4. Schematic diagram of pressure-pulsation measurement points in the pump-jet model.

For the transient simulations, one time step was assigned to every 1 deg rotation of the impeller, and a total of 20 impeller revolutions were computed. At the rated rotational speed of 600 rpm, the impeller rotational period is 0.1 s, corresponding to a time-step size of 2.7778×10^{-4} s. To reduce the influence of start-up numerical transients, the results from the 19th revolution were extracted for pressure-pulsation analysis.

The initial relative circumferential phase angle between the impeller and the guide vane was set to 0 deg in the transient calculation. It should be noted that the multiple reference frame (MRF) method was used mainly to provide an efficient and consistent numerical framework for the six comparative cases and to obtain the time-averaged flow field and mean hydrodynamic quantities, including thrust, torque, head, and efficiency, for different guide vane configurations. In contrast, the pressure-pulsation analysis was based on the transient rotor–stator calculation. In the present manuscript, no dedicated sensitivity study with multiple initial rotor–stator phase angles was performed. Therefore, the unsteady results are interpreted mainly in terms of comparative RMS level and dominant frequency among the six cases, rather than phase-specific instantaneous-flow details or absolute noise prediction. In addition, no cavitation model was activated in the present simulations. Accordingly, the low-pressure regions and low-pressure vortices discussed below only indicate potential cavitation-prone regions or vortex-shedding tendencies, and should not be directly interpreted as confirmed cavitation phenomena.

To relate the present shaftless pump-jet case to classical fluid-machinery theory, the operating condition used in the comparative simulations is first characterized by the representative flow rate $Q = VA = 10.053 \times \pi \times (0.32)^2/4 \approx 0.8085$ m^3/s. For reference, the conventional pump specific speed is defined as $N_s = nQ^{1/2}/H^{3/4}$, where n, Q, and H denote the prescribed rotational speed, representative flow rate, and computed head, respectively. In the present study, this parameter is used only as an operating-condition descriptor in the post-processing interpretation and should not be regarded as an intrinsic design classification of the thruster. Accordingly, the guide vane effect is mainly interpreted through the inlet and outlet velocity triangles of the impeller. Different guide vane handedness and motion states modify the prewhirl entering the rotor, the blade-incidence condition, and the residual circumferential velocity downstream of the rotor. These changes affect Euler-head-related energy transfer, hydraulic loss, and unsteady rotor–stator interaction, and therefore provide a classical theoretical basis for comparing the six cases.

A qualitative inlet velocity-triangle interpretation is shown in Figure 5. For the forward-inclined fixed guide vane case, the inlet circumferential velocity component is oriented in the same direction as the impeller rotation, producing positive prewhirl at the rotor inlet. This changes the relative inlet velocity and incidence angle, thereby affecting the effective flow turning across the impeller. By contrast, in the counter-rotating guide vane case, the inlet circumferential velocity component is opposite to the impeller rotation, which increases the relative flow turning and enhances Euler-head-related energy transfer. This classical velocity-triangle interpretation helps explain why different guide vane configurations lead to different head, efficiency, and pressure-pulsation characteristics.

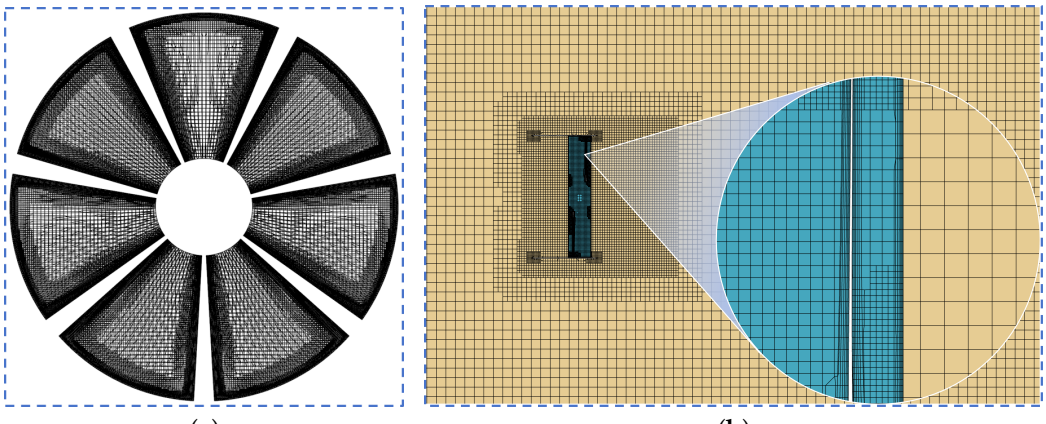


(**a**) (**b**)

Figure 5. Qualitative inlet velocity-triangle interpretation for representative guide vane configurations. (**a**) Forward-inclined fixed guide vanes. (**b**) Counter-rotating guide vanes.

2.4. Mesh Generation and Grid-Independence Verification

In the present study, the impeller operates at a relatively high rotational speed, and the thruster has a compact structure with large flow gradients. In addition, blade tips are present, where regions of high turbulence intensity are prone to form. To better support the SST $k-\omega$ turbulence model in resolving the near-field flow of the pump-jet and to improve the local spatial resolution, prism-layer meshes were generated on the impeller blade surfaces. Six prism layers were used, with a total prism-layer thickness of 0.002 m, and local mesh refinement was applied in the pump-jet region. The blade mesh of the shaftless pump-jet thruster is shown in Figure 6a, which presents a front view of the working impeller. The surrounding refined mesh region and the prism-layer mesh on the blade surfaces are shown in Figure 6b, where the prism layers on the impeller surface are enlarged on the right-hand side of the figure.



(**a**) (**b**)

Figure 6. Blade mesh (**a**) and locally refined mesh (**b**).

To minimize the potential effect of mesh density on the numerical simulation results, a mesh independence study was first performed using the full-flow-domain pump-jet model of Case 1 without a flow-guiding device. The computational domain was discretized with structured hexahedral meshes, and six mesh cases with different densities were generated by specifying different base sizes. In addition to the impeller head, the root-mean-square value of the pressure-fluctuation coefficient, $C_{p,\mathrm{RMS}}$, was also selected as a monitoring parameter to evaluate the sensitivity of both the global hydrodynamic performance and the local unsteady pressure response to mesh refinement. The relative change in each parameter was calculated as the absolute difference between the current mesh case and the preceding mesh case divided by the value of the preceding mesh case. As shown in Table 4, the impeller head gradually decreases and approaches a stable value as the mesh is refined [24]. When the total number of cells increases from 1,385,729 in Mesh 4 to 1,886,392 in Mesh 5 and 2,693,842 in Mesh 6, the relative change in head decreases to 0.32% and 0.13%, respectively. A similar convergence tendency is observed for $C_{p,\mathrm{RMS}}$. Although the pressure-fluctuation RMS is more sensitive to mesh refinement than the head, its relative change also decreases progressively with increasing mesh density, from 13.25% in Mesh 4 to 6.25% in Mesh 5 and 4.44% in Mesh 6.

Because the full six-level grid-refinement study is computationally expensive for all guide vane configurations, the detailed grid-independence verification was first performed using Case 1. To further confirm that the final mesh is also suitable for the other guide vane configurations, an additional cross-case mesh check was conducted for Cases 2–6 by comparing the adopted mesh with a refined mesh under the same reference operating condition. The comparison focused on the main integral performance parameters and the pressure-fluctuation RMS value, which are the primary quantities discussed in this study.

Table 4. Grid-independence verification.

Mesh Case	Impeller Cells	Total Cells	Head/(m)	Change in Head	$C_{p,\mathrm{RMS}}$	Change in $C_{p,\mathrm{RMS}}$
Mesh 1	409,372	689,624	1.658		0.0024	
Mesh 2	493,030	853,673	1.635	1.39%	0.00202	15.83%
Mesh 3	578,739	1,043,561	1.602	2.02%	0.00166	17.82%
Mesh 4	759,073	1,385,729	1.586	1.00%	0.00144	13.25%
Mesh 5	985,015	1,886,392	1.581	0.32%	0.00135	6.25%
Mesh 6	1,372,585	2,693,842	1.578	0.13%	0.00129	4.44%

As shown in Table 5, the additional cross-case mesh check provides further evidence for the suitability of the adopted mesh for the remaining guide vane configurations. For Cases 2–6, the relative changes in head from Mesh 4 to Mesh 5 are 0.62%, 0.30%, 0.27%, 0.20%, and 0.56%, respectively, indicating that the global hydrodynamic performance shows weak sensitivity to further mesh refinement. The pressure-fluctuation RMS is more sensitive to local mesh refinement than the head, as expected for an unsteady local quantity. For most cases, the relative change in $C_{p,\mathrm{RMS}}$ decreases when the mesh is refined from Mesh 4 to Mesh 5 compared with the change from Mesh 3 to Mesh 4. Although the $C_{p,\mathrm{RMS}}$ difference remains relatively larger in Case 2, the comparison among Mesh 3, Mesh 4, and Mesh 5 provides additional support for the stability of the pressure-pulsation trend assessment under the adopted mesh strategy.

Before analyzing the unsteady pressure fluctuation, the temporal resolution of the transient simulation was examined because the pressure-fluctuation characteristics are closely related to the periodic rotor–stator interaction. To ensure that the unsteady pressure signal was sufficiently resolved, the time step was defined according to the impeller rotation period. The rotation period is expressed as

$$T_{\mathrm{rot}} = \frac{1}{n}, \tag{9}$$

where n is the rotational speed in revolutions per second. Several time-step sizes were tested by dividing one impeller revolution into different numbers of time steps. The corresponding time step is given by

$$\Delta t = \frac{T_{\mathrm{rot}}}{N_t}, \tag{10}$$

where N_t is the number of time steps per impeller revolution.

Table 5. Additional cross-case mesh check for Cases 2–6 under the reference condition.

Case	Mesh Case	Head (m)	Change in Head	$C_{p,\mathrm{RMS}}$	Change in $C_{p,\mathrm{RMS}}$
Case 2	Mesh 3	1.5943		0.01232	
Case 2	Mesh 4	1.5844	0.62%	0.00888	27.92%
Case 2	Mesh 5	1.5802	0.62%	0.00736	17.12%
Case 3	Mesh 3	1.8992		0.08930	
Case 3	Mesh 4	1.8782	1.11%	0.05892	34.02%
Case 3	Mesh 5	1.8725	0.30%	0.06029	2.33%
Case 4	Mesh 3	1.098		0.00884	
Case 4	Mesh 4	1.0898	0.75%	0.00765	13.46%
Case 4	Mesh 5	1.0869	0.27%	0.00702	8.24%
Case 5	Mesh 3	1.4383		0.00193	
Case 5	Mesh 4	1.4234	1.04%	0.00162	16.06%
Case 5	Mesh 5	1.4205	0.20%	0.00169	4.32%
Case 6	Mesh 3	1.9090		0.02380	
Case 6	Mesh 4	1.8955	0.71%	0.01891	20.59%
Case 6	Mesh 5	1.8849	0.56%	0.01692	10.58%

The head, thrust, torque, and root-mean-square value of pressure fluctuation were selected as the evaluation indicators. As shown in Table 6, when the time step was gradually refined, the variations in the main hydrodynamic quantities and pressure-fluctuation RMS became smaller. Considering both numerical accuracy and computational cost, $T_{\mathrm{rot}}/360$ was finally adopted for the subsequent transient simulations.

Table 6. Time-step independence verification for the transient simulation.

Time Step	Head/(m)	Thrust/(N)	Pressure-Fluctuation RMS
$T_{\mathrm{rot}}/90$	1.700	709.517	0.1830
$T_{\mathrm{rot}}/180$	1.634	705.919	0.1260
$T_{\mathrm{rot}}/360$	1.586	700.276	0.0998
$T_{\mathrm{rot}}/720$	1.599	698.723	0.0962

After the temporal resolution was determined, the mesh sensitivity of the unsteady pressure fluctuation was further evaluated. Although the pump head was used as the primary indicator in the mesh independence verification, it mainly reflects the overall hydraulic performance. To assess whether the mesh resolution is also sufficient for predicting local unsteady pressure characteristics, the pressure-fluctuation coefficient history during the 19th rotational period was compared among different mesh cases at a representative monitoring location. As shown in Figure 7, the coarser meshes (Mesh 1–Mesh 3) exhibit relatively irregular short-wavelength oscillations and sharper local peaks, indicating that the predicted local pressure signal is still affected by insufficient spatial resolution. By contrast, the fluctuation histories obtained using Mesh 4–Mesh 6 become markedly smoother and more repeatable, and the overall waveform, phase evolution, and amplitude level show only minor differences among these finer meshes.

To quantitatively evaluate the mesh sensitivity of the unsteady pressure signal, the root-mean-square value of the fluctuating pressure coefficient was calculated after removing its mean component:

$$C_{p,\mathrm{RMS}} = \sqrt{\frac{1}{N}\sum_{i=1}^{N}(C_{p,i} - \overline{C_p})^2}, \tag{11}$$

where $C_{p,i}$ is the instantaneous pressure coefficient, $\overline{C_p}$ is its time-averaged value over the selected sampling period, and N is the number of sampling points.

The RMS values of the pressure coefficient obtained using Mesh 4, Mesh 5, and Mesh 6 were 0.00633, 0.00660, and 0.00634, respectively. The relative difference between Mesh 4 and Mesh 6 was only 0.12%, and the maximum relative difference among the three fine meshes was less than 5%. Therefore, further mesh refinement had only a limited influence on the predicted pressure-pulsation level, and Mesh 4 was considered sufficient for resolving the pressure-pulsation characteristics while maintaining reasonable computational cost.

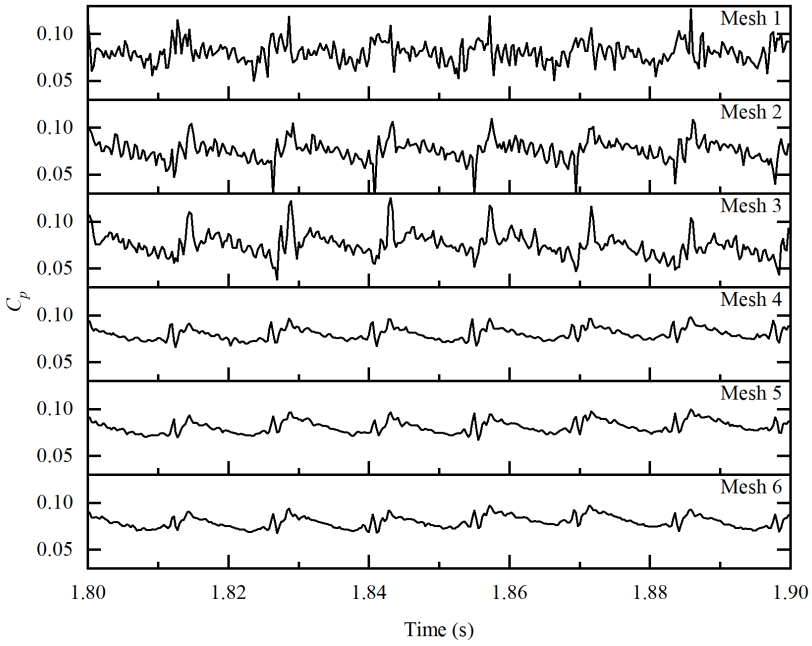


Figure 7. Comparison of the pressure-coefficient fluctuation histories during the 19th rotational period under different mesh cases.

This additional comparison indicates that, although the pump head already provides a useful global criterion, local fluctuating variables are more sensitive to mesh resolution and therefore should also be considered in the grid-independence assessment. Similar observations have been reported in previous numerical studies, which noted that insufficient resolution or grid-refinement-related numerical effects may introduce spurious pressure oscillations, artificial noise, or dispersion-related distortion in local fluctuation signals, especially when unsteady quantities are analyzed [25]. Therefore, in the present work, the final mesh was selected not only based on the convergence of the pump head, but also based on the stabilization of the local pressure-coefficient fluctuation history. Considering both computational accuracy and cost, the meshing criterion of Case 4 was ultimately adopted as the mesh standard for the present numerical simulations.

Because direct experimental data for the present shaftless pump-jet thruster with rotating guide vanes are not yet available, additional literature-based evidence was introduced to support the reasonableness of the adopted numerical framework. Previous experimental/numerical studies on pump-jet propulsion have shown that CFD predictions

of hydrodynamic force and noise can agree well with towing-tank and cavitation-tunnel measurements [5]. For shaftless water-jet propulsion pumps, RANS simulations with the SST $k-\omega$ turbulence model in closely related shaftless water-jet propulsion pumps have been compared with experimental head and cavitation-performance data, with reported deviations generally below 5% [9]. In addition, studies on integrated motor pump-jet thrusters and ducted propellers have shown that RANS-based calculations, grid-convergence analysis, and transient sliding-mesh treatment can provide reasonable predictions of hydrodynamic loads and rotor–stator interaction in compact rotating propulsion systems [12]. Therefore, although direct experimental validation of the present case remains necessary in future work, the adopted numerical framework is consistent with validated approaches reported for closely related pump-jet and ducted propulsor systems.

3. Results and Discussion

Before analyzing the hydrodynamic performance and pressure-pulsation characteristics, the stability of the transient calculation was examined by taking the typical pump-jet model with vertical guide vanes under a propeller rotational speed of 600 rpm as a representative case. As shown in Figure 8, the instantaneous velocity contours at the same rotor phase during the 5th, 10th, 15th, and 20th revolutions indicate that the flow field induced by the pump-jet develops gradually and becomes essentially stable after approximately the 15th revolution.

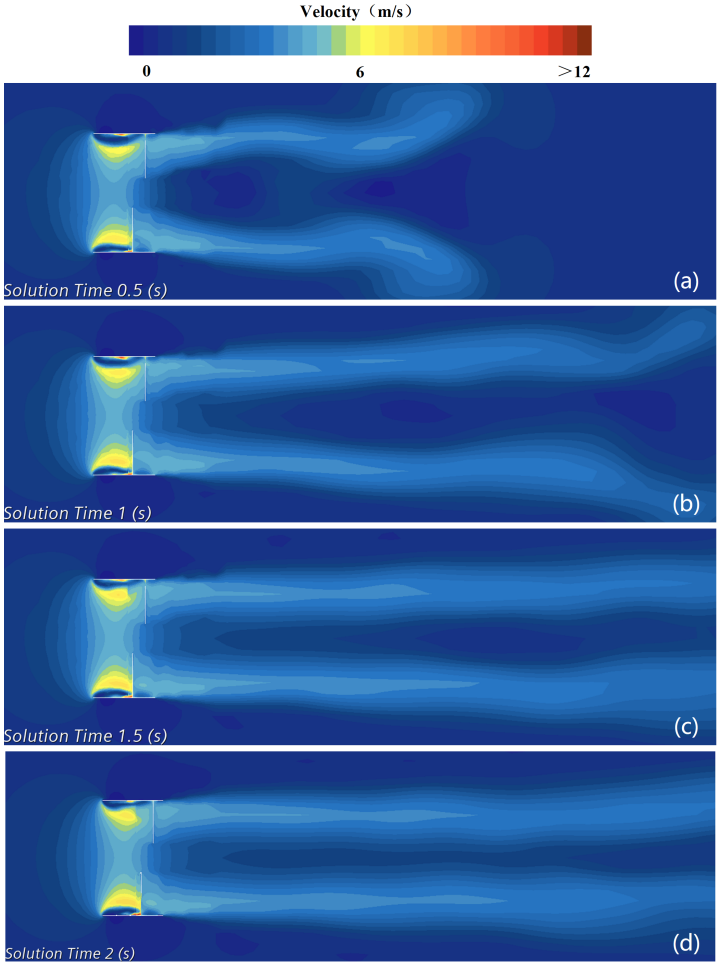


Figure 8. Instantaneous velocity contours of the typical pump-jet model with vertical guide vanes at different solution times under a propeller rotational speed of 600 rpm: (**a**) 0.5 s, (**b**) 1.0 s, (**c**) 1.5 s, and (**d**) 2.0 s.

In addition, the pressure-pulsation histories at monitoring point M2 during the 18th, 19th, and 20th revolutions are compared in Figure 9. The adjacent stable revolutions exhibit good cycle-to-cycle repeatability, indicating that the pressure fluctuation has reached a stable periodic state. Therefore, the data from the 19th revolution were selected as representative data from the stable stage for the subsequent analysis of hydrodynamic performance, pressure pulsation, and frequency-domain characteristics.

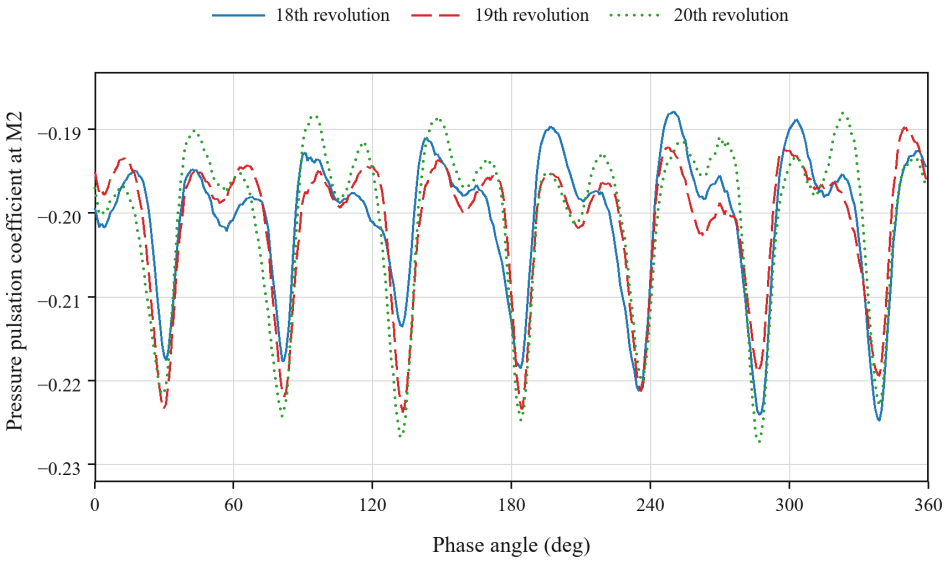


Figure 9. Cycle-to-cycle comparison of the pressure-pulsation coefficient at monitoring point M2 during the 18th, 19th, and 20th revolutions for the typical pump-jet model with vertical guide vanes under a propeller rotational speed of 600 rpm.

3.1. Comparison of Six Cases Under the Reference Condition

3.1.1. Energy Performance Analysis

The thrust coefficient is a dimensionless parameter used to characterize the propulsion capability of a water-jet pump. It provides a direct measure of the thrust performance of the pump. To compare the effects of guide vane case on the axial thrust characteristics of the working impeller in the shaftless pump-jet thruster, the axial thrust coefficient K_{TH} was employed in this study to evaluate thrust performance. The axial thrust coefficient is calculated as follows:

$$K_{TH} = \frac{T_h}{\rho n^2 D^4} \tag{12}$$

where T_h is the axial force acting on the blades (N); ρ is the density of water (kg/m³); n is the rotational speed of the impeller (r/min); and D is the impeller diameter (m).

To intuitively characterize the transient variation in the thrust coefficient of the working impeller under different guide vane orientations, 360 instantaneous sampling points were extracted from the 19th cycle, and the time-domain curves of the thrust coefficient for each case were obtained, as shown in Figure 10. It can be seen that the thrust coefficients in all cases exhibit pronounced periodic fluctuations, although substantial differences exist in both fluctuation amplitude and mean level among the cases. Case 3 shows the highest overall thrust coefficient and the most intense periodic oscillation, indicating that this case can generate relatively large axial thrust but with comparatively poor thrust-output stability.

Cases 2, 4, and 6 exhibit intermediate thrust-coefficient levels and relatively distinct periodic variations. By contrast, Cases 1 and 5 show gentler variations and smaller overall fluctuation amplitudes. These results indicate that different guide vane orientations not

only affect the magnitude of the working impeller thrust coefficient, but also significantly alter its unsteady fluctuation characteristics.

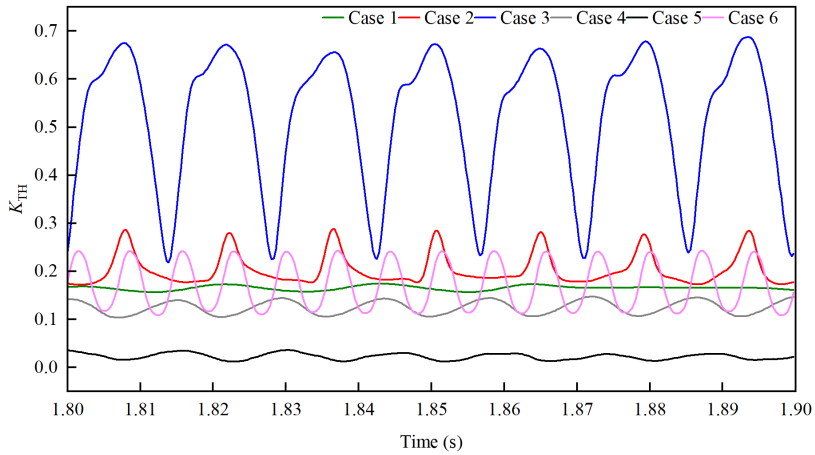


Figure 10. Time-domain variation in thrust coefficient under different cases.

Figure 11 presents a box-and-whisker plot showing the distribution of the axial thrust coefficient of the pump-jet impeller at 600 rpm for the six cases. The data were extracted from 360 sampling points in the 19th rotational period. As shown in Figure 11, the thrust coefficients of Case 1 and Case 5 are highly concentrated around 0.17 and 0.02, respectively. In the study by Tan et al. [20] on the influence of blade number on the performance of a shaftless pump-jet thruster, the axial thrust coefficient was reported to be approximately 0.19 when the blade number was seven, which provides a useful reference for the present study. For Case 3, in which the fixed guide vane has the same blade handedness as the working impeller, the thrust coefficient exhibits the largest interquartile range, approximately 0.22, with a median value of about 0.57. The square inside each box represents the mean value for the corresponding dataset.

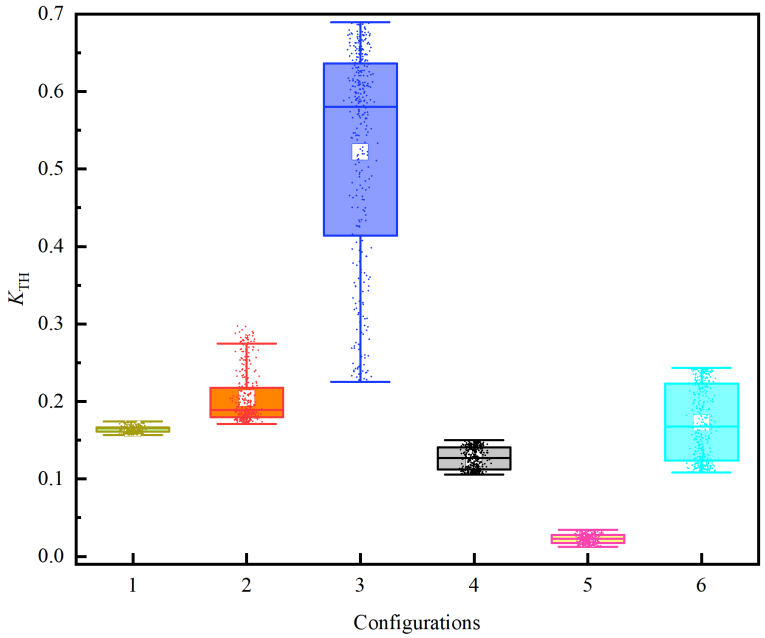


Figure 11. Thrust coefficient of the rotor under each case.

3.1.2. Head and Efficiency Comparison

In addition to the thrust coefficient, the energy conversion capability of the propulsion device is also an important indicator for evaluating the merits of different guide vane orientations. Under the conditions without a guide device and with a fixed guide device, the working impeller is the only active power-input component in the system. Therefore, the propulsion efficiency can be described using the classical expression for a single rotating propulsor, namely

$$\eta = \frac{TV_A}{Q_r\,\omega_r} = \frac{(K_{TH}\rho n^2 D^4)\cdot(JnD)}{(K_Q\rho n^2 D^5)\cdot(2\pi n)} = \frac{K_{TH}J}{2\pi K_Q} \tag{13}$$

where V_A denotes the inflow velocity; Q_r and ω_r denote the torque and angular velocity of the working impeller, respectively; K_{TH} is the thrust coefficient; K_Q is the torque coefficient; and $J = V_A/(nD)$ is the advance coefficient. This expression shows that the propulsion efficiency essentially reflects the capability of the device to convert the input shaft power into effective propulsive power.

$$\eta = \frac{T_{\text{net}}V_A}{Q_r\omega_r + Q_g\omega_g} \tag{14}$$

It should be noted that when the guide device is in a rotating state, namely in Cases 5 and 6, the upstream guide device itself also participates in energy exchange, and its power input cannot be neglected. Therefore, for these two dynamically rotating guide vane configurations, the reported propulsion efficiency represents the overall efficiency of the complete pump-jet device, with the input powers of both the working impeller and the rotating guide vane included. This definition is used consistently when comparing the six configurations, and the efficiency is calculated as follows:

$$\eta = \frac{T_{\text{net}}V_A}{P_r + P_g} = \frac{T_{\text{net}}V_A}{Q_r\omega_r + Q_g\omega_g} \tag{15}$$

where P_r is the input power of the working impeller, and P_g is the input power of the rotating guide vane; Q_g and ω_g are the torque and angular velocity of the rotating guide device, respectively, and T_{net} is the net thrust of the device. In other words, if only the thrust and torque of the working impeller are substituted into the classical efficiency formula, the obtained result is more suitable as a relative evaluation index for the energy characteristics of the working impeller, and cannot be regarded as fully equivalent to the overall propulsion efficiency of the complete device including the input power of the rotating guide device. Since this study focuses on comparing the effects of different guide device orientations on the hydrodynamic performance and flow-field pressure characteristics of the shaftless pump-jet, the comprehensive performance of each case is further analyzed below in combination with energy-characteristic parameters such as head and efficiency.

Figure 12 presents the numerically simulated head and efficiency of the working impeller in the shaftless pump-jet under different cases. As shown in Figure 12, the pump-jet model in Case 6 achieves the highest head, reaching 1.8955 m, followed by Case 3 with a head of 1.8782 m, whereas Case 4 exhibits the lowest head of 1.0898 m. Figure 6 also shows that Case 6 yields the highest efficiency, reaching 0.7306, followed by Case 5 with an efficiency of 0.641, while Case 4 has the lowest efficiency of 0.0221. In particular, the efficiency of Case 2 with the fixed vertical guide vane case is 59.46%, which is close to the efficiency of 61.91% reported by Qin et al. [26] in their experimental study on the hydrodynamic performance of a pump-jet propulsor with a pre-swirl stator. This agreement provides a limited consistency check for the magnitude of the predicted efficiency.

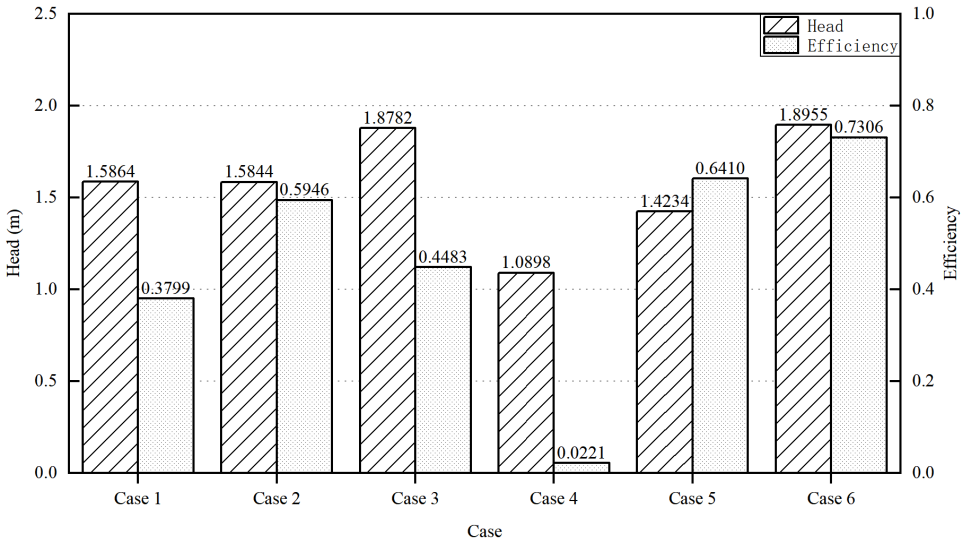


Figure 12. Energy performance metrics for each case.

3.1.3. Vortex Structure

Coherent vortex structures in the wake are not only direct products of flow separation and shear-layer evolution, but also important manifestations of energy redistribution and dissipation. The integrity of their topology and the stability of their evolution directly determine the hydraulic efficiency of the propulsor [27]. In shaftless pump-jet systems in particular, the interference between the guide device and the impeller can significantly alter the generation mechanism and breakdown path of the wake vortex system, thereby affecting the energy conversion efficiency of the propulsor [28]. To quantitatively reveal the influence of different guide device orientations on the wake energy reorganization mechanism, the vortex-core regions were extracted using the Q-criterion. The Q-criterion, originally introduced by Hunt et al. [29], identifies vortical regions from the second invariant of the velocity-gradient tensor by distinguishing rotation-dominated regions from strain-dominated regions. This definition is suitable for visualizing coherent vortex structures in complex three-dimensional wakes. In addition, Chakraborty et al. [30] discussed the relationships among several local vortex-identification cases and showed that such criteria provide a useful basis for interpreting vortex topology and flow-structure evolution. Therefore, the Q-criterion was adopted here to compare the wake vortex organization, vortex breakdown, and downstream energy redistribution under different guide device cases.

Figure 13 shows the visualization results of the vortical isosurfaces at $Q = 120\ s^{-2}$, where Cases 1–6 correspond to the six guide device cases. Under the condition without a guide device, the wake vortex structure of Case 1 retains a basic helical morphology; however, owing to the absence of the rectifying effect of a guide device, the vortex core undergoes pronounced distortion and diffusion in the mid-wake region. In Case 2, the fixed vertical guide vanes significantly improve the stability of the wake structure, forming a strongly coherent helical vortex that extends throughout the entire computational domain. This indicates that the coherent wake structure is well preserved, with relatively weak vortex breakdown and dissipation. In Case 3, with a co-directionally fixed guide device, coherent vortices are observed in the wake, but they tend to break down and disintegrate, reflecting the development of vortex instability and turbulent dissipation during downstream transport. In Case 4, with a counter-directionally fixed guide device, the vortex structure is severely fragmented, and only indistinct vortical clusters remain in the near-field region. This suggests that the counter-directionally fixed guide device intensifies the flow interference between the impeller and the guide device, causing rapid

dissipation of the wake structure within a very short distance. In Case 5, the co-rotating guide device rotates synchronously with the impeller, thereby reducing relative motion and alleviating local flow separation. In Case 6, with a counter-rotating guide device, the wake vortex structure is clear, is compact, and continuously extends into the far field, indicating a highly organized wake with minimal disordered dissipation. This behavior is consistent with the higher head and efficiency obtained for this case.

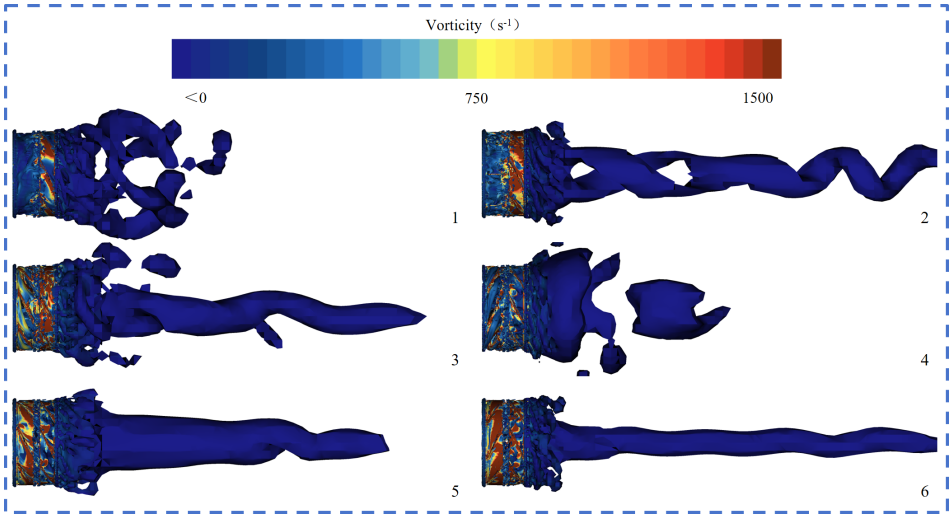


Figure 13. Vortex structures of the pump-jet under different guide device cases.

3.1.4. Pressure Distribution

After the solution reached a stable state, the axial pressure distributions in the fluid domain of the shaftless pump-jet thruster for the six cases were obtained, as shown in Figure 14. The label in the lower-right corner of each subfigure denotes the corresponding case. Overall, the axial pressure distributions indicate a common flow pattern among the cases: the fluid is drawn in from the low-pressure region near the inlet, accelerated and pressurized by the impeller to form a high-pressure region in the core flow passage, and finally discharged at high velocity to generate thrust, followed by the formation of a low-pressure wake downstream.

Further analysis shows that Case 1 exhibits a relatively uniform axial pressure distribution, with a smooth pressure transition inside the pump-jet. A distinct low-pressure region appears on the suction surface of the impeller blades, and the outlet wake presents a clustered structure. In Case 2, the axial pressure gradient is relatively mild, and only a slight low-pressure region appears near the impeller inlet. This may be attributed to the presence of the fixed vertical guide vanes, which inhibits the development of the low-pressure region. The wake is elongated and relatively symmetric. In Case 3, the axial pressure field exhibits strong unsteady flow features. Several pronounced low-pressure clusters and spots appear near the duct inlet and between the guide vanes and the impeller. These low-pressure spots can be regarded as potential cavitation-sensitive regions or locations associated with vortex-structure evolution. The wake is slender and exhibits lateral deflection. In Case 4, no distinct low-pressure region is observed in the axial pressure field, and no complex pressure variation occurs inside the pump-jet; however, the wake is relatively long and wide. For Cases 5 and 6, distinct low-pressure regions appear on the suction surfaces of the guide vanes near the duct inlet, while the internal pressure field varies relatively smoothly. The wake in Case 5 is longer and more regular, whereas Case 6 produces the shortest wake.

These observations provide useful insight into how different guide vane orientations affect the internal flow dynamics and pressure distribution of the pump-jet, as well as the resulting overall performance and efficiency.

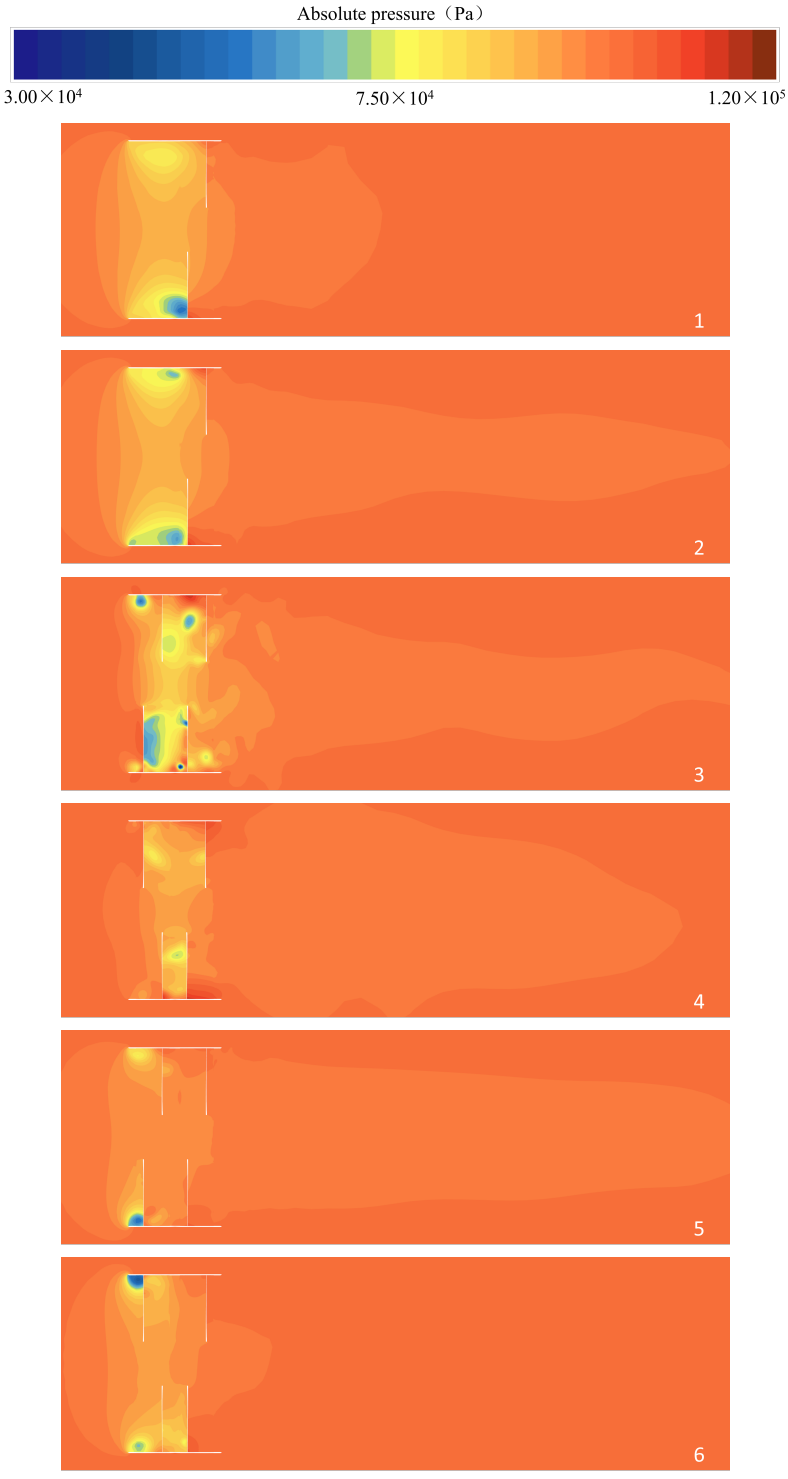


Figure 14. Axial pressure distribution for different cases. The numbers 1–6 denote Cases 1–6, respectively.

Figure 15 shows the pressure contours on the suction surface of the working impeller blades for the different pump-jet cases. As shown in Figure 15, in Cases 1, 2, and 6, the pressure on the blade suction surface decreases counterclockwise from the blade tip toward the blade root. In Cases 3 and 4, the pressure on the suction surface of the working impeller first decreases and then increases from the blade tip to the blade root, while it gradually increases from the leading edge to the trailing edge, with the lowest pressure occurring near the leading edge. Local low-pressure vortical structures appear on the blade surface, and this phenomenon is most pronounced in Case 3, indicating a potential risk of flow separation

or cavitation in this region. By contrast, Case 5 exhibits the most uniform instantaneous pressure distribution in the selected flow field, indicating a relatively smooth spatial pressure field. The corresponding pressure-fluctuation characteristics are further evaluated using the monitoring-point signals and RMS pressure coefficients in the following sections.

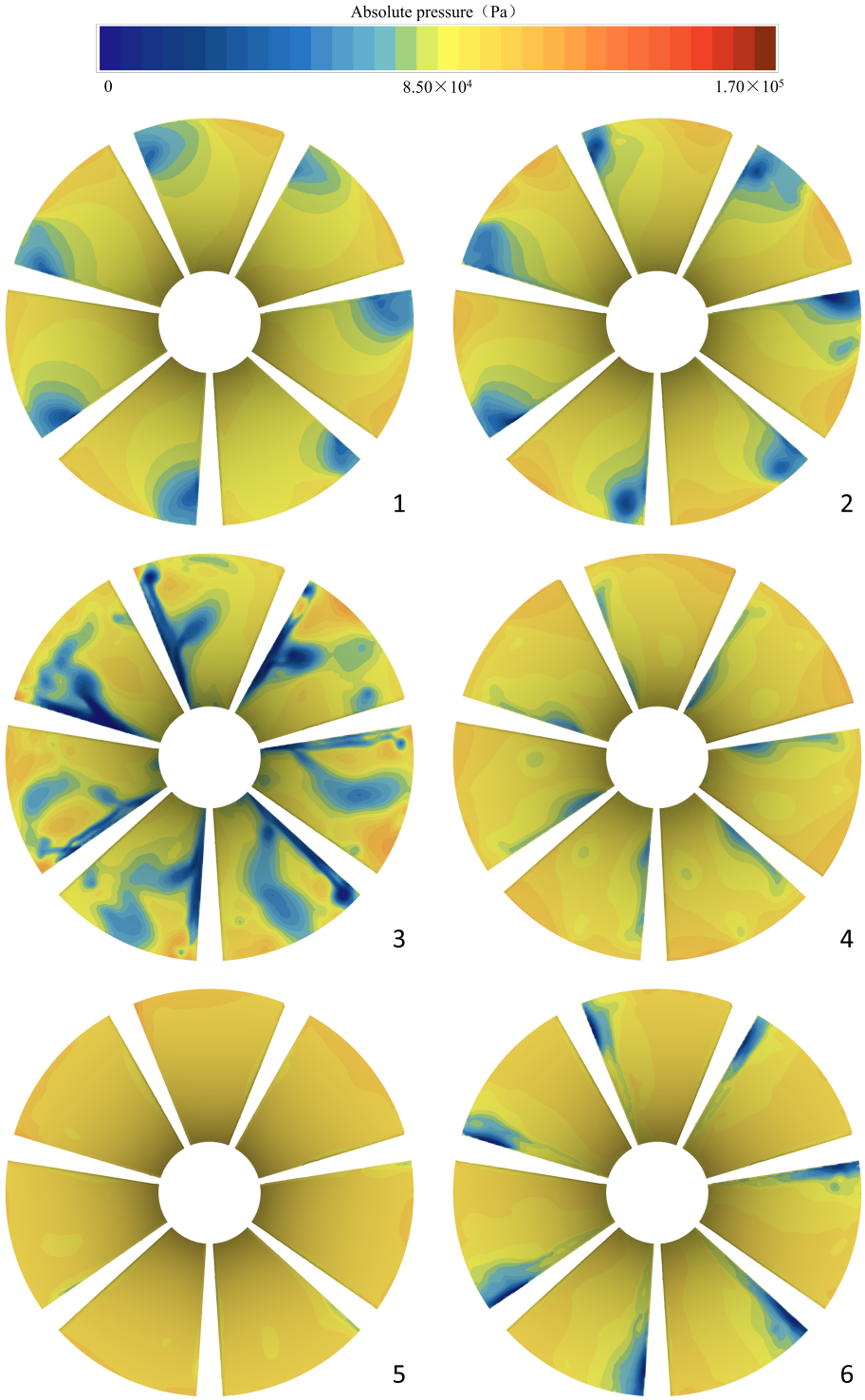


Figure 15. Pressure distribution on the suction surface of the rotor blades for different cases. The numbers 1–6 denote Cases 1–6, respectively.

3.1.5. Pressure-Pulsation Analysis

Figure 16 compares the root-mean-square values of the pressure coefficient obtained at the three monitoring points for each shaftless pump-jet thruster case during the 19th

rotational period. As shown in Figure 16a–c, the pressure-pulsation coefficient generally decreases from the impeller rim (M1) toward the central axis (M3) for all six cases, although the values at M3 are slightly higher than those at M2 in Cases 1, 2, 4, and 5. In addition, for each individual monitoring-point series, Case 3 exhibits the largest RMS value of C_p, substantially exceeding those of the other cases, indicating that the pressure fluctuation is strongest in the monitored regions for this case. At monitoring point M2, Case 1 shows the lowest RMS value of C_p, followed by Case 5 with a slightly higher value. Moreover, Case 5 yields the lowest effective C_p values among all cases at both M1 and M3.

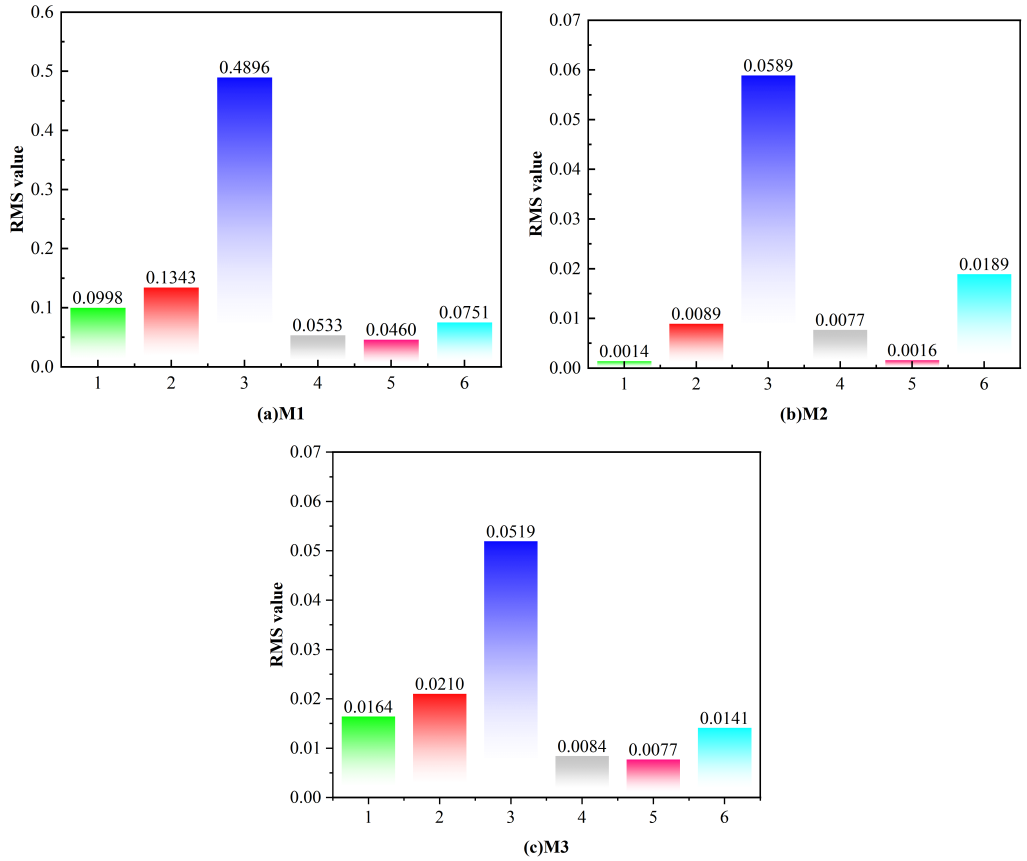


Figure 16. Root-mean-square pressure coefficient for each case.

To facilitate a comprehensive comparison of the energy performance and pressure-pulsation characteristics of the six simplified guide vane configurations under the reference operating condition, Table 5 summarizes the head, efficiency, and root-mean-square values of the pressure coefficient at M1, M2, and M3 for all cases. As shown in Table 7, under this reference condition, Case 6 exhibits the best energy performance among the six configurations, but it does not correspond to the lowest pressure-pulsation level. Conversely, Case 5, which shows relatively weak pressure pulsations, is not advantageous in terms of head or efficiency. This indicates that guide vane case optimization under the present simplified geometric and operating conditions requires a simultaneous trade-off between propulsion performance and unsteady pressure response. Although Case 3 achieves a relatively high head, its pressure pulsations at all three monitoring points are significantly higher than those of the other cases, suggesting that enhancing energy output alone may be accompanied by stronger flow instability. By comparison, Case 6 achieves the highest head and efficiency while maintaining a lower pressure-pulsation level than Case 3 under the reference operating condition, indicating favorable overall performance within the present six-case comparison.

Table 7. Summary of hydrodynamic performance and RMS pressure coefficients.

Case	Head/m	Efficiency	RMS Cp at M1	RMS Cp at M2	RMS Cp at M3
Case 1	1.5864	0.3799	0.0998	0.0014	0.0164
Case 2	1.5844	0.5946	0.1343	0.0089	0.0210
Case 3	1.8782	0.4483	0.4896	0.0589	0.0519
Case 4	1.0898	0.0221	0.0533	0.0077	0.0084
Case 5	1.4234	0.6410	0.0460	0.0016	0.0077
Case 6	1.8955	0.7306	0.0751	0.0189	0.0141

3.1.6. Frequency-Domain Analysis of Pressure Pulsations

Fast Fourier transform (FFT) was applied to the pressure-pulsation coefficient data extracted from the 19th revolution at the three monitoring points for each case. The time-domain signals were decomposed into linear combinations of sine and cosine components at different frequencies. By calculating the amplitude and phase information of these components, the pressure-pulsation coefficient at each monitoring point was represented in the frequency domain. The mean component was removed from the frequency-domain data.

As shown in Figure 17a, at monitoring point M1, the dominant pressure-pulsation frequency of all six cases is consistent with the blade-passing frequency. Among them, Case 3 exhibits a pronounced sharp peak at the dominant frequency, with the pressure-pulsation coefficient amplitude reaching 0.66, representing the strongest pulsation response among all cases. The dominant-frequency amplitudes of Cases 1, 2, and 6 are approximately 0.1, whereas those of Cases 4 and 5 are about 0.04.

As shown in Figure 17b, at monitoring point M2, the dominant pressure-pulsation frequencies of Cases 1, 2, 3, 4, and 5 coincide with the blade-passing frequency of the working impeller, whereas the dominant frequency of Case 6 is approximately twice the blade-passing frequency. Compared with M1, the pressure-pulsation peaks at the dominant frequency decrease markedly for all cases. Case 3 still exhibits the most pronounced pulsation amplitude, approaching 0.08, while Cases 1 and 5 show the smallest amplitudes, both approximately 0.001.

As shown in Figure 17c, at monitoring point M3, the dominant pressure-pulsation frequencies of Cases 1, 2, 3, 4, and 5 are also consistent with the blade-passing frequency of the working impeller, whereas Case 6 again exhibits a dominant response at approximately twice the blade-passing frequency. Compared with the dominant-frequency pressure-pulsation amplitudes at M2, the amplitudes at M3 continue to decrease for most cases, except for slight increases in Cases 1 and 2. Case 3 presents the largest pulsation amplitude at M3, reaching 0.03.

3.2. Operating-Condition Sensitivity of Representative Configurations

Based on the six-case comparison under the reference operating condition, two representative configurations were selected for the extended operating-condition sensitivity analysis: the vertical-vane configuration and the counter-rotating-vane configuration. As summarized in Table 7, among the fixed guide vane configurations, Case 2 (vertical-vane configuration) exhibits relatively high efficiency and does not produce strong pressure pulsations, and therefore, it was selected as a representative fixed guide vane configuration with balanced performance. Among the dynamically rotating guide vane configurations, Case 6 (the counter-rotating-vane configuration) showed favorable performance in most of the evaluated indicators, especially thrust and overall efficiency under the reference condition, and was therefore selected as the representative rotating guide vane configuration. By comparing these two representative configurations under the 3×3 operating-condition matrix, this section further examines how inflow velocity and rotational speed affect the

hydrodynamic performance and pressure-pulsation characteristics of different guide vane motion states.

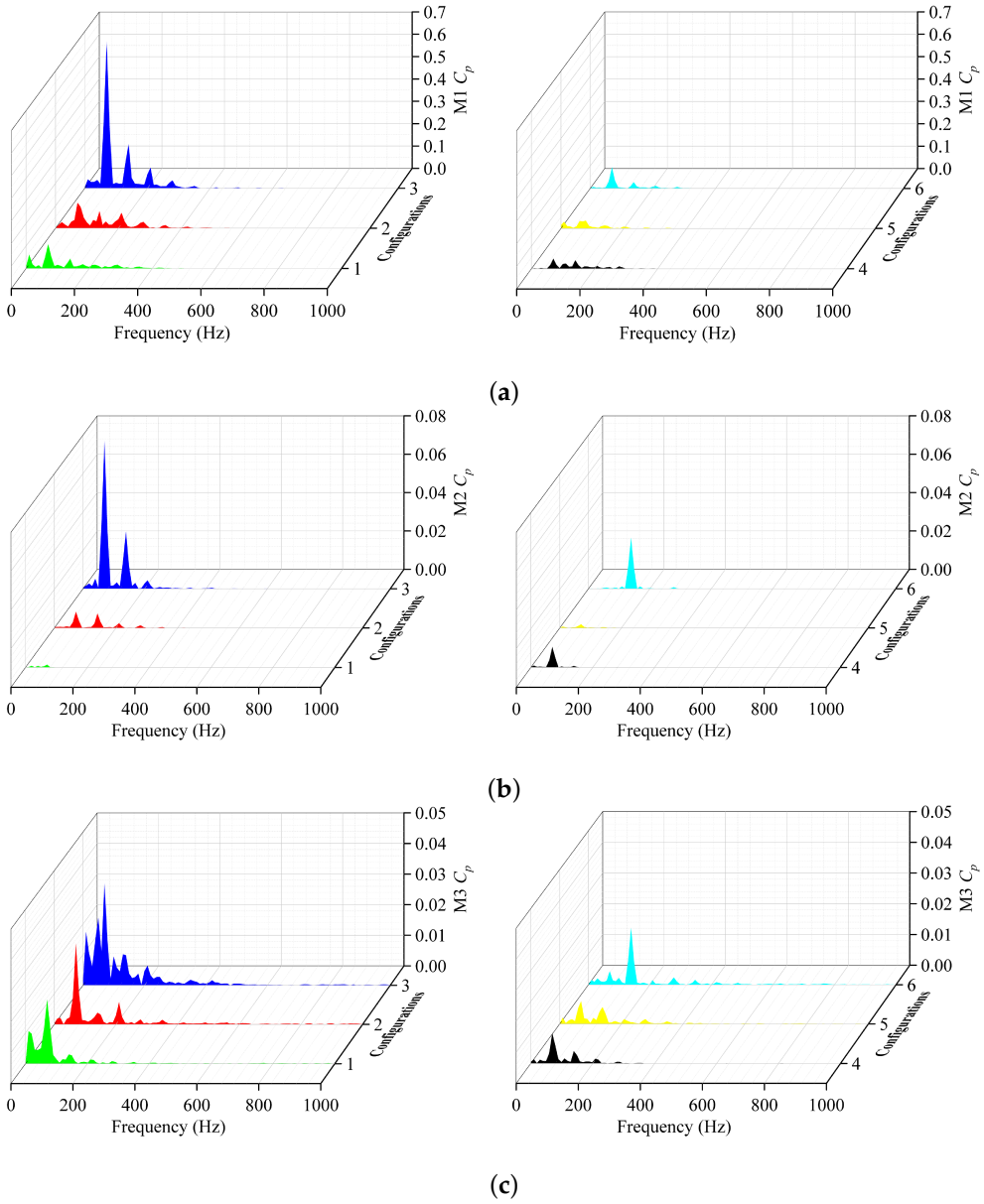


Figure 17. Pressure-fluctuation spectra at different monitoring points under different cases: (**a**) monitoring point M1; (**b**) monitoring point M2; (**c**) monitoring point M3.

A 3 × 3 operating-condition matrix was established for each representative configuration. The reference rotational speed was set as 600 rpm, and two off-reference rotational speeds, 480 rpm and 720 rpm, corresponding to $0.8\,n_{\mathrm{ref}}$ and $1.2\,n_{\mathrm{ref}}$, were additionally considered. For each rotational speed, three inflow velocities were simulated—reverse inflow, static water, and forward inflow—corresponding to −1 kn, 0 kn, and 1 kn, respectively. Here, 1 kn is equal to 0.5144 m/s.

To provide a dimensionless description of the inflow condition, the inflow velocities were converted into the advance coefficient $J = V_A/(nD)$, where V_A is the inflow velocity, n is the rotational speed in revolutions per second, and D is the characteristic diameter of the thruster. In this study, $D = 0.32$ m. Therefore, the corresponding advance coefficients are $J = -0.201, 0, 0.201$ at 480 rpm; $J = -0.161, 0, 0.161$ at 600 rpm; and $J = -0.134, 0, 0.134$ at 720 rpm. The negative J represents the reverse-inflow condition, while the positive J

represents the forward-inflow condition. The operating-condition matrix is summarized in Table 8.

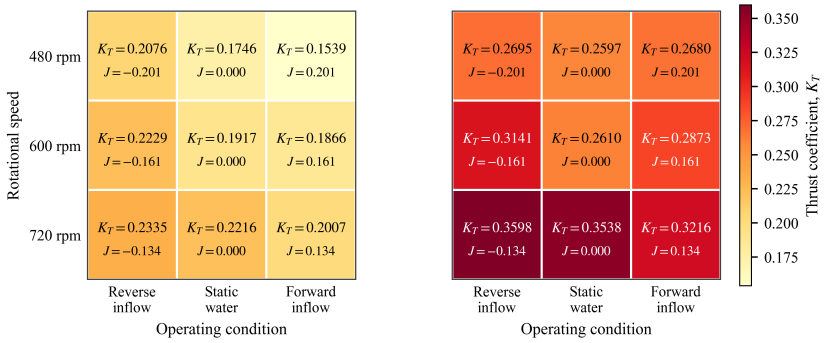
Table 8. Operating-condition matrix for the representative configurations.

Case	Rotational Speed	Advance Coefficient J	Number of Cases
Vertical-vane configuration	480, 600, 720 rpm	480 rpm: −0.201/0/0.201 600 rpm: −0.161/0/0.161 720 rpm: −0.134/0/0.134	9
Counter-rotating-vane configuration	480, 600, 720 rpm	480 rpm: −0.201/0/0.201 600 rpm: −0.161/0/0.161 720 rpm: −0.134/0/0.134	9

Based on this operating-condition matrix, the thrust coefficient, torque coefficient, thrust-to-power ratio, and pressure-fluctuation coefficient are compared in the following subsections. This arrangement allows the performance trend, power requirement, and flow stability of the two representative configurations to be evaluated beyond a single reference operating condition.

3.2.1. Thrust Coefficient

The thrust coefficient K_T was first analyzed to evaluate the thrust-generation capability of the two representative configurations under different rotational speeds and advance coefficients. As shown in Figure 18, the K_T values of both configurations vary with rotational speed and inflow condition, indicating that the thrust performance is affected by the combined influence of n and J.



(a) Vertical-vane configuration (b) Counter-rotating-vane configuration

Figure 18. Thrust coefficient distributions of the vertical-vane and counter-rotating-vane configurations under different rotational speeds and advance coefficients.

For the vertical-vane configuration, K_T increases with rotational speed under all three inflow conditions. Under the reverse-inflow condition, K_T increases from 0.2076 at 480 rpm to 0.2335 at 720 rpm. Under the static-water condition, it increases from 0.1746 to 0.2216, while under the forward-inflow condition, it increases from 0.1539 to 0.2007. This trend indicates that the vertical-vane configuration can produce higher thrust loading at higher rotational speeds. However, at the same rotational speed, the thrust coefficient under the forward-inflow condition is generally lower than that under the reverse-inflow condition, suggesting that the prescribed inflow direction changes the effective blade loading and the axial momentum increase through the thruster.

For the counter-rotating-vane configuration, the thrust coefficient is significantly higher than that of the vertical-vane configuration over the entire operating range. The K_T value increases from 0.2695 to 0.3598 under the reverse-inflow condition, from 0.2597 to

0.3538 under the static-water condition, and from 0.2680 to 0.3216 under the forward-inflow condition as the rotational speed increases from 480 rpm to 720 rpm. The maximum K_T of 0.3598 is obtained at 720 rpm under the reverse-inflow condition. Even the minimum K_T of the counter-rotating-vane configuration is higher than the maximum K_T of the vertical-vane configuration, which indicates stronger thrust-generation capability within the investigated operating range.

To further quantify the difference between the two configurations, the relative increase in thrust coefficient is defined as

$$\Delta K_T = \frac{K_{T,\mathrm{CRV}} - K_{T,\mathrm{VV}}}{K_{T,\mathrm{VV}}} \times 100\%, \tag{16}$$

where $K_{T,\mathrm{CRV}}$ and $K_{T,\mathrm{VV}}$ denote the thrust coefficients of the counter-rotating-vane and vertical-vane configurations, respectively.

According to the calculated results, the counter-rotating-vane configuration produces a higher K_T than the vertical-vane configuration in all nine operating conditions. The relative increase ranges from 29.8% to 74.1%, with an average improvement of approximately 50.9%. The largest improvement occurs at 480 rpm under the forward-inflow condition, where K_T increases from 0.1539 to 0.2680. This indicates that the thrust-enhancement effect of the counter-rotating-vane configuration is not limited to the reference operating condition, but remains evident under off-reference rotational speeds and inflow conditions.

The improvement in K_T can be attributed to the stronger interaction between the impeller wake and the counter-rotating guide vanes. Compared with the vertical-vane configuration, the counter-rotating-vane arrangement is more effective in modifying the circumferential velocity component and enhancing the axial momentum increase of the flow, thereby producing a larger pressure difference and thrust output. Nevertheless, a higher thrust coefficient does not necessarily indicate better overall hydrodynamic performance, since the corresponding torque requirement, power consumption, and pressure-fluctuation characteristics must also be considered. Therefore, the torque coefficient and unsteady pressure fluctuation are further analyzed in the following subsections.

3.2.2. Pressure-Fluctuation Characteristics in the Frequency Domain

Although the counter-rotating-vane configuration shows a clear advantage in thrust coefficient, the improvement in thrust performance may be accompanied by changes in unsteady pressure excitation. Therefore, the pressure-fluctuation characteristics in the frequency domain were further analyzed to evaluate the flow stability of the two representative configurations.

In this study, two representative operating conditions were selected for the frequency-domain comparison. The first one is the low-speed forward-inflow condition, namely 480 rpm with $J = 0.201$, and the second one is the high-speed reverse-inflow condition, namely 720 rpm with $J = -0.134$. For the 480 rpm condition, the shaft frequency is

$$f_s = \frac{480}{60} = 8 \text{ Hz}.$$

Since the impeller has seven blades, the blade-passing frequency is

$$f_{\mathrm{BPF}} = Z f_s = 7 \times 8 = 56 \text{ Hz}.$$

The corresponding second-order blade-passing frequency is therefore $2f_{BPF} = 112$ Hz. Similarly, for the 720 rpm condition, the shaft frequency is

$$f_s = \frac{720}{60} = 12 \text{ Hz},$$

and the blade-passing frequency is

$$f_{BPF} = 7 \times 12 = 84 \text{ Hz},$$

with the second-order blade-passing frequency located at 168 Hz.

Figure 19 shows the pressure-fluctuation spectra at three monitoring points, M1, M2, and M3. Figure 19a,c,e correspond to the spectra at 480 rpm with $J = 0.201$, while Figure 19b,d,f correspond to those at 720 rpm with $J = -0.134$. The dominant spectral components are mainly concentrated in the low-frequency range, especially near the shaft frequency, the blade-passing frequency, and their harmonic components. This indicates that the pressure fluctuation is mainly governed by the periodic rotor–stator interaction and the passage of the impeller blades.

At 480 rpm, clear spectral peaks can be observed near the blade-passing frequency of 56 Hz. In some monitoring positions, additional peaks also appear near the second-order blade-passing frequency of 112 Hz, indicating that the pressure fluctuation is not purely sinusoidal but contains higher-order periodic components induced by the interaction between the impeller wake and the guide vane region. At monitoring point M1, the vertical-vane configuration shows a pronounced dominant peak, whereas the counter-rotating-vane configuration reduces the amplitude of the main low-frequency component. This suggests that the counter-rotating-vane arrangement can weaken the local periodic pressure excitation near M1 under the low-speed forward-inflow condition.

At 720 rpm, the characteristic frequencies shift to higher values. The blade-passing frequency increases to 84 Hz, and the second-order blade-passing frequency appears near 168 Hz. Compared with the 480 rpm condition, the spectra under 720 rpm contain more evident characteristic peaks, especially around the blade-passing frequency and its harmonic components. This indicates that the higher rotational speed and reverse-inflow condition strengthen the unsteady rotor–stator interaction. In particular, the occurrence of clear peaks near $2f_{BPF}$ suggests that higher-order periodic pressure excitation becomes more important under the high-load reverse-inflow condition.

For monitoring point M2, the overall pressure-fluctuation amplitude is much lower than that at M1, but the characteristic peaks near the blade-passing frequency and its harmonic components can still be identified. Under the 720 rpm condition, the counter-rotating-vane configuration exhibits a relatively distinct peak near the second-order blade-passing frequency, indicating that the counter-rotating guide vanes may enhance local periodic excitation at this monitoring position.

At monitoring point M3, the frequency-domain response shows a stronger dependence on the guide vane configuration. Under the 480 rpm condition, the vertical-vane configuration presents a relatively strong low-frequency component, while the counter-rotating-vane configuration redistributes the pressure-fluctuation energy toward the blade-passing-related frequency range. Under the 720 rpm condition, the counter-rotating-vane configuration produces a more noticeable peak near the blade-passing frequency or its harmonic component, suggesting that the counter-rotating arrangement intensifies the periodic interaction between the impeller wake and the downstream flow field in some local regions.

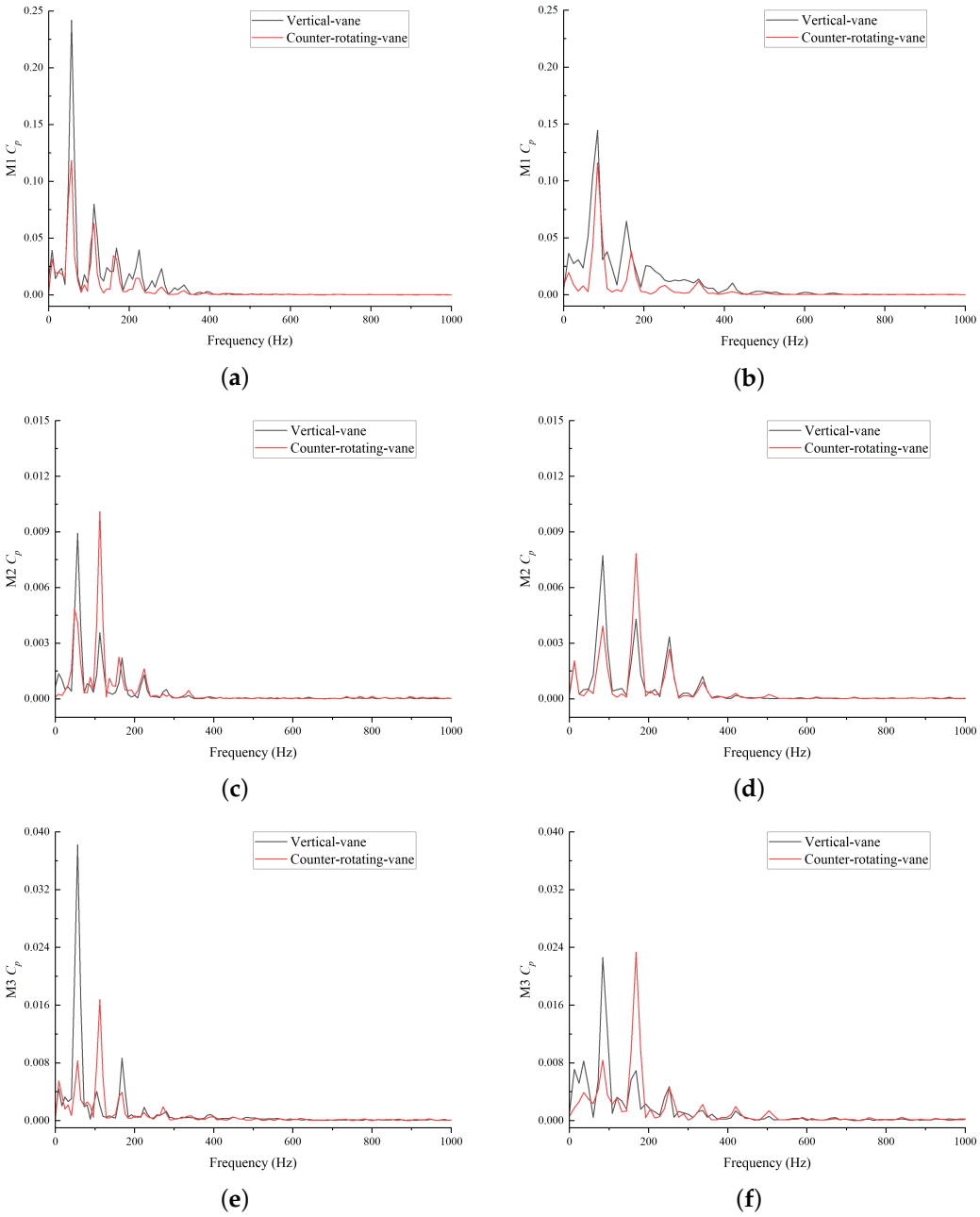


Figure 19. Frequency-domain pressure-fluctuation characteristics at different monitoring points. Subfigures (**a**,**c**,**e**) show the pressure-fluctuation spectra at 480 rpm, while subfigures (**b**,**d**,**f**) show the corresponding spectra at 720 rpm.

Overall, the extended operating-condition analysis indicates that the counter-rotating-vane configuration maintains favorable hydrodynamic performance compared with the representative vertical-vane configuration under the selected off-reference conditions. Meanwhile, the frequency-domain results show that the pressure fluctuation is closely related to the shaft frequency, blade-passing frequency, and their harmonic components. Although the counter-rotating-vane configuration improves the thrust coefficient under the investigated operating conditions, it also changes the distribution of pressure-fluctuation energy in the frequency domain. In some regions, it reduces the dominant low-frequency pressure fluctuation, whereas in other regions, especially under the high-speed reverse-inflow condition, it may enhance the blade-passing-frequency or double-blade-passing-frequency components. Therefore, the hydrodynamic advantage of the counter-rotating-vane configu-

ration should be evaluated together with its influence on unsteady pressure excitation and flow stability.

3.3. Rotor–Stator Interaction Mechanism and Higher-Order Harmonic Excitation

The frequency-domain results indicate that the pressure fluctuation is mainly governed by the periodic rotor–stator interaction between the impeller wake and the guide vane passages. For the reference condition of 600 rpm, the shaft frequency is 10 Hz and the blade-passing frequency is 70 Hz. In the extended operating-condition analysis, the blade-passing frequency shifts to 56 Hz at 480 rpm and 84 Hz at 720 rpm. The spectral peaks observed near these characteristic frequencies indicate that the periodic blade-passing process is a dominant source of pressure fluctuation.

Compared with the vertical-vane configuration, the counter-rotating-vane configuration changes the relative motion between the impeller outlet wake and the guide vane passages. The increased relative tangential velocity strengthens the periodic wake impingement on the guide vanes and promotes stronger local rotor–stator interaction. As a result, the pressure-fluctuation energy is redistributed in the frequency domain, and peaks near the second-order blade-passing frequency can be observed at some monitoring points. This indicates that the double-blade-passing-frequency component is not an independent excitation source, but a higher-order harmonic response caused by enhanced periodic interaction.

Therefore, the counter-rotating-vane configuration improves thrust generation, but it may also introduce more complex harmonic characteristics in local pressure fluctuation. The present results should be interpreted mainly as comparative evidence of how guide vane motion affects rotor–stator interaction and spectral composition, rather than as an absolute prediction of broadband noise.

3.4. Limitations and Future Work

Although the present study has been extended from a single reference condition to a multi-condition analysis of representative configurations, several limitations remain. First, the six guide vane configurations were compared under the same reference condition, while the extended operating-condition sensitivity analysis was conducted only for the vertical-vane and counter-rotating-vane configurations. This two-stage strategy is appropriate for identifying representative trends while controlling computational cost, but a complete operating map for all configurations has not yet been established.

Second, the present work is still based on numerical simulation. The numerical credibility is supported by grid-independence verification, time-step setting based on the impeller rotation period, pressure-fluctuation mesh-sensitivity analysis, and comparison with validated numerical/experimental studies on closely related pump-jet and ducted propulsor systems. However, direct experimental validation of the present shaftless pump-jet thruster with rotating guide vanes has not yet been completed. Therefore, the results should be interpreted primarily as comparative hydrodynamic and pressure-fluctuation trends among different configurations and operating conditions, rather than as absolute experimentally validated predictions.

Third, cavitation, fluid–structure interaction, electromagnetic excitation from the rim motor, and full-scale installation effects were not included in the present model. These factors may influence local pressure fluctuation, structural vibration, and radiated noise under practical operating conditions. Future work will focus on open-water experiments, dynamic pressure measurements, and further validation of the predicted pressure-fluctuation characteristics. Cavitation effects and coupled fluid–structure responses should also be

considered to assess the hydrodynamic and acoustic performance of shaftless pump-jet thrusters more comprehensively.

4. Conclusions

This study numerically investigated the impeller performance, internal pressure distribution, and pressure-pulsation characteristics of a shaftless pump-jet thruster under six guide vane cases. For the simplified surrogate blade geometries considered in this study, and based on the reference-condition comparison of six guide vane configurations and the extended operating-condition analysis of the representative vertical-vane and counter-rotating-vane configurations, the following conclusions can be drawn.

- The guide vane case has a significant influence on the energy performance of the impeller. The counter-rotating guide vane case achieves the highest head and efficiency, reaching 1.8955 m and 0.7306, respectively, whereas the fixed reverse-inclined guide vane case yields the lowest head and efficiency, at 1.0898 m and 0.0221, respectively. Compared with the fixed vertical guide vane case, the counter-rotating guide vane case increases the head and efficiency by 19.64% and 22.87%, respectively. The fixed forward-inclined guide vane case exhibits a relatively high thrust coefficient, but also shows the most pronounced thrust fluctuation, indicating poor load stability.
- The extended 3×3 operating-condition analysis shows that the counter-rotating-vane configuration maintains a higher thrust coefficient than the vertical-vane configuration under all investigated rotational speeds and inflow conditions, indicating that its thrust-enhancement effect is not limited to the reference condition. Specifically, the counter-rotating-vane configuration produces a higher K_T than the vertical-vane configuration in all nine operating conditions, with the relative increase ranging from 29.8% to 74.1%. This result indicates that the hydrodynamic advantage of the counter-rotating-vane configuration remains observable under off-reference rotational speeds and inflow conditions.
- Different guide vane cases modify the low-pressure regions inside the pump-jet and the pressure distribution on the suction surface of the impeller blades. In the fixed forward-inclined guide vane case, distinct local low-pressure regions and unsteady flow structures are formed between the guide vanes and the impeller and near the suction surface of the impeller blades, indicating that this case is more prone to inducing strong pressure disturbances. In Cases 5 and 6, the internal pressure transition is relatively smooth; in particular, Case 6 produces a shorter wake, which is beneficial for reducing downstream non-uniform disturbances. Since no cavitation model was adopted in this study, the low-pressure regions can only be interpreted as potential cavitation-prone regions or vortex-shedding tendencies, and cannot be directly identified as cavitation.
- The pressure-pulsation intensity generally decreases in the radial direction from the impeller rim toward the central axis. The fixed forward-inclined guide vane case presents the largest root-mean-square pressure coefficient values at M1, M2, and M3, which are 0.4896, 0.0589, and 0.0519, respectively, indicating the strongest pressure fluctuations. The co-rotating guide vane case exhibits relatively weak pressure pulsations at M1 and M3, showing favorable pulsation suppression capability. By contrast, Case 6 exhibits a response at twice the blade-passing frequency at M2 and M3. This response is mainly attributed to the counter-rotation of the guide vanes, which increases the relative passing frequency and strengthens wake–passage interaction. This finding provides preliminary comparative insight into the optimization of low-pulsation guide vane configurations for simplified pump-jet geometries.

- The frequency-domain analysis shows that, in most cases, the dominant pressure-pulsation frequency is consistent with the blade-passing frequency of 70 Hz. The counter-rotating guide vane case exhibits a dominant response at approximately twice the blade-passing frequency at M2 and M3. This phenomenon is associated with the higher relative passing frequency between the counter-rotating guide vanes and the impeller, indicating that the motion state of the guide vanes not only affects the pressure-pulsation amplitude but also changes the spectral composition of the internal pressure fluctuations.

Author Contributions: Conceptualization, T.W. and S.S.; methodology, T.W., S.S. and L.L.; software, T.W., S.S., L.L. and J.Y.; validation, all authors contributed to validation; resources, S.S.; data curation, T.W. and S.S.; writing—original draft preparation, T.W., S.S. and L.L.; writing—review and editing, all authors were engaged in reviewing and editing the current version; supervision, S.S.; project administration, S.S. and K.L.; funding acquisition, S.S. All authors have read and agreed to the published version of the manuscript.

Funding: The work is supported by the Shenzhen Fundamental Research (Key Program) under Grant JCYJ20241202124931042, the Key Science and Technology Project of the Shenzhen Science and Technology Innovation Commission (SSTIC) under Grant No. KJZD20230923115505011, the cluster special project "development of intelligent detection and sampling device for deep sea mineral resources" of Shenzhen Institutes of Advanced Technology, Chinese Academy of Sciences, under Grant JQ0101-2025/02, the technology innovation project of China National Offshore Oil Company (CNOOC) under grant (202612484183), and the outsourced project of Ocean Development Planning Research Center of Guangdong Province (No.GPCGD253109FG064F).

Data Availability Statement: The original contributions presented in this study are included in the article material. Further inquiries can be directed to the corresponding author.

Conflicts of Interest: The authors declare no conflicts of interest.

References

1. Li, Q.; Abdullah, S.; Rasani, M.R.M. A review of progress and hydrodynamic design of integrated motor pump-jet propulsion. *Appl. Sci.* **2022**, *12*, 3824. [CrossRef]
2. Zhu, H.; Jin, S.; Wang, D.; Wei, Y.; Hu, P.; Wu, X.; He, S.; Hu, F. Open-water characteristics of shaftless pump-jet thruster. *Acta Armamentarii* **2021**, *42*, 835.
3. Wang, C.; Weng, K.; Guo, C.; Chang, X.; Gu, L. Analysis of influence of duct geometrical parameters on pump jet propulsor hydrodynamic performance. *J. Mar. Sci. Technol.* **2020**, *25*, 640–657. [CrossRef]
4. Liu, H.; Zhao, Y.; Tan, M.; Hua, R.; Wu, X. Radiated noise from cavitation bubble volume pulsation in a shaftless pump-jet propulsor. *Proc. Inst. Mech. Eng. Part A J. Power Energy* **2025**, *239*, 295–306. [CrossRef]
5. Weng, K.; Sun, C.; Han, K.; Wang, C.; Sun, S.; Li, P.; Hu, J. Experimental/numerical investigation on the hydrodynamic and noise characteristics of pump-jet propulsion. *Ocean Eng.* **2024**, *307*, 117995. [CrossRef]
6. He, S.; Zhou, F. Hydrodynamics design and tests of clearance flow in bearings of shaftless pump-jet thrusters. *China Mech. Eng.* **2022**, *33*, 406.
7. Shen, Y.; Hu, P.; Jin, S.; Wei, Y.; Lan, R.; Zhuang, S.; Zhu, H.; Cheng, S.; Chen, J.; Wang, D.; et al. Design of novel shaftless pump-jet propulsor for multi-purpose long-range and high-speed autonomous underwater vehicle. *IEEE Trans. Magn.* **2016**, *52*, 7403304 . [CrossRef]
8. Cao, P.; Wang, Y.; Li, G.; Qian, X. Research on the performance of shaftless water-jet propulsion. In Proceedings of the ASME 2014 4th Joint US-European Fluids Engineering Division Summer Meeting, Chicago, IL, USA, 3–7 August 2014.
9. Lei, J.; Wang, Y.; Liu, H.; Li, M.; Pi, Q. Investigation of cavitation flow field and flow loss in shaftless water-jet propulsion pump under different acceleration conditions. *J. Mar. Sci. Eng.* **2025**, *13*, 2165. [CrossRef]
10. Han, W.; Chen, Y.; Xue, T.; Lei, P. The impact of pump cavity gaps on the flow characteristics of helical mixed-flow pumps. *Actuators* **2025**, *14*, 444. [CrossRef]
11. Zhu, Z.; Liu, H. The external characteristics and inner flow research of rim-driven thruster. *Adv. Mech. Eng.* **2022**, *14*, 16878132221081608. [CrossRef]

12. Li, Q.; Abdullah, S.; Rasani, M.R.M. Hydrodynamic performance of an integrated motor pump-jet thruster with gap flow effects. *J. Mar. Sci. Technol.* **2024**, *29*, 789–811. [CrossRef]
13. Huang, W.; Wang, X.; Xu, L.; Wang, W.; Yan, J.; He, J. Marine fouling roughness effects on pump-jet hydrodynamics and flow noise. *Phys. Fluids* **2026**, *38*. [CrossRef]
14. Yevtushenko, A.A.; Kochevsky, A.N.; Fedotova, N.A.; Schelyaev, A.Y.; Konshin, V.N. Investigation of flow inside an axial-flow pump of GV-IMP type. *arXiv* **2004**, arXiv:physics/0411186.
15. Binama, M.; Kan, K.; Chen, H.-X.; Zheng, Y.; Zhou, D.; Su, W.-T.; Muhirwa, A.; Ntayomba, J. Flow instability transferability characteristics within a reversible pump turbine (RPT) under large guide vane opening (GVO). *arXiv* **2021**, arXiv:2107.10462.
16. Nouri, H.; Ravelet, F.; Bakir, F.; Sarraf, C.; Rey, R. Design and experimental validation of a ducted counter-rotating axial-flow fans system. *arXiv* **2012**, arXiv:1208.6396.
17. Odetti, A.; Altosole, M.; Bruzzone, G.; Caccia, M.; Viviani, M. Design and construction of a modular pump-jet thruster for autonomous surface vehicle operations in extremely shallow water. *J. Mar. Sci. Eng.* **2019**, *7*, 222. [CrossRef]
18. Zhang, Q.; Jaiman, R.K.; Ma, P.; Liu, J. Investigation on the performance of a ducted propeller in oblique flow. *arXiv* **2018**, arXiv:1801.03211.
19. Karassik, I.J.; Messina, J.P.; Cooper, P.; Heald, C.C. *Pump Handbook*, 4th ed.; McGraw-Hill: New York, NY, USA, 2008.
20. Tan, M.; Hu, S.; Liu, H.; Ma, H.; Zhu, Z. Influence of blade number on performance of hubless pump-jet thruster. *J. Natl. Univ. Def. Technol.* **2024**, *46*, 212–221.
21. Menter, F.R. Two-equation eddy-viscosity turbulence models for engineering applications. *AIAA J.* **1994**, *32*, 1598–1605. [CrossRef] [PubMed]
22. Li, P.; Mu, J.; Wang, Z.; Wang, C. Numerical study of the wake evolution behind a shaftless pump-jet propulsor. *Appl. Ocean Res.* **2025**, *165*, 104854. [CrossRef]
23. Wang, T.; Li, W.; Zang, W.; Song, S. SAC-Based Strategy Solving for Reservoir Pollutant Source Tracing by AUV. In *Proceedings of the CCF Intelligent Vehicles Symposium*; Springer Nature: Singapore, 2025; pp. 353–364.
24. Xiang, Y.; Wang, W. Hydrodynamic performance evaluation of pump-jet propulsion based on the toroidal propeller. *Ocean Eng.* **2024**, *311*, 118932. [CrossRef]
25. Ching, E.J.; Johnson, R.F.; Kercher, A.D. A note on reducing spurious pressure oscillations in fully conservative discontinuous Galerkin simulations of multicomponent flows. *arXiv* **2023**, arXiv:2310.17792.
26. Qin, D.; Huang, Q.; Pan, G.; Li, F.; Han, P. Experimental study of hydrodynamic performances of pre-swirl pump-jet propeller. *J. Northwest. Polytech. Univ.* **2023**, *41*, 601–611. [CrossRef]
27. Yu, H.; Zhang, Z.; Hua, H. Numerical investigation of tip clearance effects on propulsion performance and pressure fluctuation of a pump-jet propulsor. *Ocean Eng.* **2019**, *192*, 106500. [CrossRef]
28. Sun, Y.; Peng, H.; Liu, W.; Guo, J.; Guo, Y. Comparison of the hydrodynamic performance of front and rear-stator pump-jet propulsors in an oblique wake under the cavitation condition. *Phys. Fluids* **2022**, *34*. [CrossRef]
29. Hunt, J.C.R.; Wray, A.A.; Moin, P. Eddies, streams, and convergence zones in turbulent flows. In *Proceedings of the Summer Program 1988*; Center for Turbulence Research, Stanford University: Stanford, CA, USA, 1988; pp. 193–208.
30. Chakraborty, P.; Balachandar, S.; Adrian, R.J. On the relationships between local vortex identification cases. *J. Fluid Mech.* **2005**, *535*, 189–214. [CrossRef]

Disclaimer/Publisher's Note: The statements, opinions and data contained in all publications are solely those of the individual author(s) and contributor(s) and not of MDPI and/or the editor(s). MDPI and/or the editor(s) disclaim responsibility for any injury to people or property resulting from any ideas, methods, instructions or products referred to in the content.